

1 **Bowen ratio-constrained global dataset of bulk air-sea turbulent**  
2 **heat fluxes from 1993 to 2017**

3 Yizhe Wang<sup>a, b</sup>, Ronglin Tang<sup>a, b, \*</sup>, Meng Liu<sup>c</sup>, Lingxiao Huang<sup>a, b</sup>, Zhao-Liang Li<sup>a, b, c</sup>

4 <sup>a</sup> State Key Laboratory of Resources and Environment Information System, Institute of  
5 Geographic Sciences and Natural Resources Research, Chinese Academy of Sciences,  
6 Beijing 100101, China

7 <sup>b</sup> University of Chinese Academy of Sciences, Beijing 100049, China

8 <sup>c</sup> State Key Laboratory of Efficient Utilization of Arable Land in China, Institute of  
9 Agricultural Resources and Regional Planning, Chinese Academy of Agricultural  
10 Sciences, Beijing 100081, China

11 \* Authors to whom correspondence should be addressed: tangrl@reis.ac.cn

12

13

14

## 15 **Abstract**

16 Air-sea turbulent heat fluxes, including the sensible heat flux (SHF) and latent heat  
17 flux (LHF), along with the Bowen ratio ( $\beta$ , ratio of SHF to LHF), are crucial for  
18 understanding air-sea interaction and global energy and water budgets. However, the  
19 existing products, primarily developed using the semi-empirical bulk aerodynamic  
20 methods and data-driven machine learning approaches, are often weak in accuracy and  
21 physical rationality, due to the uncertainties in the environmental forcings and  
22 inappropriate parameterizations. In this study, we generated a global daily  $0.25^\circ$  product  
23 of bulk air-sea turbulent heat fluxes using the Bowen ratio-constrained Neural Network  
24 (NN) model (referred to as the BrTHF model) that could coordinately estimate the SHF  
25 and LHF, along with the observations from 197 globally distributed buoys and multi-  
26 source remote sensing and reanalysis inputs. The spatial ten-fold cross-validation  
27 results showed that the BrTHF model, achieving root mean square errors of  $6.05 \text{ W/m}^2$ ,  
28  $23.67 \text{ W/m}^2$  and  $0.22$  and correlation coefficients of  $0.93$ ,  $0.91$  and  $0.25$  for the SHF,  
29 LHF and  $\beta$ , respectively, outperformed the physics-agnostic NN model and seven  
30 widely used air-sea turbulent heat flux products (including JOFURO3, IFREMER,  
31 SeaFlux, ERA5, MERRA2, OAFflux, and OHF). Furthermore, the inter-comparison of  
32 the spatial distribution of multi-year means, as well as intra-annual and inter-annual  
33 change patterns showed that the BrTHF product reliably simulated global SHF, LHF  
34 and  $\beta$ , in contrast to the machine learning-based OHF product that failed to replicate  
35 these patterns. The main advantage of the BrTHF model lies in its improved rationality  
36 of  $\beta$  estimates, successfully eliminating the outliers observed in the physics-agnostic  
37 NN model and the seven typical products. The improved SHF, LHF, and  $\beta$  estimates  
38 can allow for more accurate quantification of the global air-sea energy and water  
39 budgets, enhance our understanding of air-sea interaction, and improve projections of  
40 climate change under global warming. The  $0.25^\circ$  daily global product from 1993 to  
41 2017 can be freely accessed from the National Tibetan Plateau Data Center (TPDC)  
42 [<https://doi.org/10.11888/Atmos.tpdc.302578>, Tang and Wang (2025)].

43 **Keywords:** Air-sea turbulent heat fluxes; Sensible heat flux; Latent heat flux; Bowen  
44 ratio

## 45 **1. Introduction**

46 Air-sea turbulent heat fluxes, comprising the latent heat flux (LHF) and sensible  
47 heat flux (SHF), play vital roles in the Earth's climate system by characterizing the  
48 exchange of energy and water between the ocean and atmosphere (Wild et al., 2014;  
49 Loeb et al., 2021; Fasullo et al., 2014). Accurate estimation of SHF, LHF and their  
50 ratio—the Bowen ratio ( $\beta = \text{SHF}/\text{LHF}$ ) is an essential prerequisite for advancing our  
51 understanding of atmosphere-sea interaction (Gentemann et al., 2020), improving the  
52 quantification of global water and energy budget (Zhang, 2023), and enhancing the  
53 predictability of extreme weather events (Yu, 2019).

54 To estimate global air-sea turbulent heat fluxes, the semi-empirical bulk  
55 aerodynamic method was developed based on the Monin-Obukhov similarity theory  
56 (Monin and Obukhov, 1954). It establishes scaling relationships between fluxes and  
57 near-surface meteorological variables such as wind speed, humidity, and temperature  
58 (Yu, 2019). This method, for its ease of application, has been applied to generate tens  
59 of widely used products in the past few decades (Shie et al., 2009; Liman et al., 2018;  
60 Yu and Weller, 2007; Berry and Kent, 2011; Tomita et al., 2018; Crespo et al., 2019).  
61 However, there were huge discrepancies in the global and regional magnitude and  
62 patterns of SHF and LHF among these products, which seriously impeded our  
63 understanding of the key process of the air-sea interaction and the global budget of  
64 water and energy (Bentamy et al., 2017; Tang et al., 2024; Yu, 2019). The discrepancies  
65 could be partly attributed to the substantial uncertainties in the environmental forcings  
66 used to develop these products (Robertson et al., 2020) and the inappropriate  
67 parameterizations (Brodeau et al., 2017; Jiang et al., 2024a; Jiang et al., 2024b; Yang et  
68 al., 2024). More explicitly, existing parameterizations often rely on simplified  
69 assumptions about atmospheric stability and boundary layer dynamics, which may not  
70 hold under diverse environmental conditions. For instance, most bulk algorithms are

71 optimized for moderate wind regimes, resulting in degraded performance and increased  
72 uncertainty when applied under weak wind regimes (Jiang et al., 2024a; Brunke, 2002).  
73 At very high wind speeds, however, observations show that the drag coefficient can  
74 decrease due to sea spray and whitecap formation, reducing effective surface roughness  
75 and potentially biasing flux estimates (Cai et al., 2025). In addition, simplifications in  
76 the treatment of sea surface skin temperature, saturation humidity, and air density in the  
77 parameterizations can also introduce substantial uncertainty (Brodeau et al., 2017).  
78 Together, these limitations can contribute a lot to the biases in the SHF and LHF  
79 estimates which can even lead to the unphysical estimations of  $\beta$ , as Wang et al. (2024)  
80 reported. To better describe and comprehend the air-sea interaction and the energy and  
81 water budgets, the existing mode to produce global air-sea turbulent heat fluxes needs  
82 improvement urgently.

83 Machine learning techniques have been extensively applied to upscale point-scale  
84 in-situ measurements of a single variable (such as soil moisture, roughness, or  
85 temperature) into grid-scale global datasets (Wang et al., 2023; Peng et al., 2022; O and  
86 Orth, 2021; Nelson et al., 2024; Fu et al., 2023). These efforts highlight the great  
87 potential of machine learning for more accurate and consistent multivariate coordinated  
88 mapping (Karniadakis et al., 2021; Kashinath et al., 2021; Van Der Westhuizen et al.,  
89 2023; Wang et al., 2024). However, the application of machine learning in global  
90 mapping of air-sea turbulent heat fluxes remains limited. Among these studies, some  
91 have focused on solely improving the accuracy of LHF, while the remaining studies  
92 have mostly considered independent modeling of SHF and LHF (Bourras et al., 2007;  
93 Cummins et al., 2024; Cummins et al., 2023; Zhou et al., 2024). In both approaches,  
94 however, most studies have not produced long-term flux products. The only publicly  
95 available machine learning-based global air-sea turbulent heat fluxes product, released  
96 by the National Oceanic and Atmospheric Administration (NOAA) Ocean heat flux  
97 CDR (hereafter dubbed OHF), simultaneously modeled SHF and LHF using a Neural  
98 Network (NN) technique (Clayson and Brown, 2016). Although it performed well when

99 validated against the observations from the tropical buoys, it failed to capture the  
100 regional characteristics, particularly in areas where air-sea turbulent heat exchange is  
101 intense (e.g. oceans with latitudes beyond  $45^\circ$  for SHF and subtropical highs for LHF)  
102 (Tang et al., 2024). Additionally, it exhibited different patterns of temporal evolution of  
103 global annual mean and opposite inter-annual trends at both regional and global scales  
104 to most widely-used physical model-based products, likely due to unreasonable  
105 construction of observation datasets [with data before and after 2007 coming from  
106 SeaFlux in-situ datasets and ICOADS (International Comprehensive Ocean-  
107 Atmosphere Data Set) datasets, respectively]. Furthermore, the product likely suffers  
108 from unphysical estimates of the  $\beta$  due to neglecting the interrelations among SHF, LHF  
109 and  $\beta$  during the model construction.

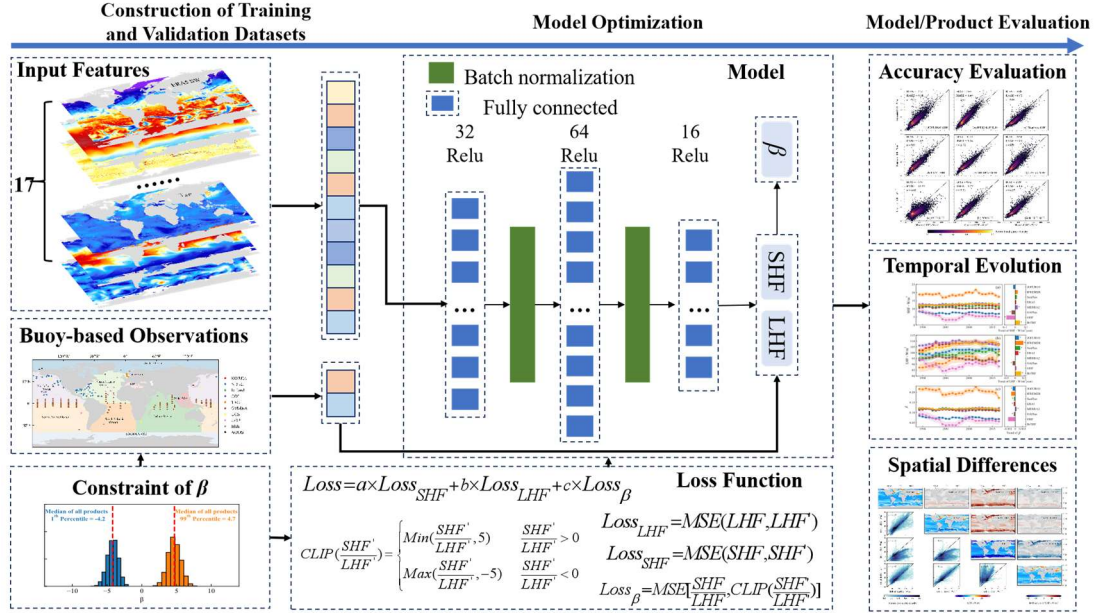
110 To improve the estimation of SHF, LHF, and  $\beta$  in a coordinative framework, we  
111 recently proposed an innovative Bowen ratio-informed data-driven model by  
112 considering the synergistic changes [on the one hand, ensuring physical consistency  
113 (i.e.,  $\text{SHF}/\text{LHF} = \beta$ ); on the other hand, achieving high-accuracy estimations of SHF,  
114 LHF, and  $\beta$  simultaneously] using a Random Forest (RF) technique (Wang et al., 2024).  
115 Validation against hourly eddy covariance (EC) flux measurements from 53 historical  
116 cruises demonstrated the model's superior performance, achieving high accuracy in  
117 estimating SHF, LHF, and  $\beta$ , with results that are physically consistent. Wang et al.  
118 (2024) highlights the feasibility of simultaneously estimating SHF, LHF, and  $\beta$  with  
119 high accuracy using machine learning techniques, offering strong potential for global  
120 mapping that aligns with physical consistency. However, since EC observations are  
121 difficult to obtain at sea due to platform motion and airflow distortion (Bourras et al.,  
122 2019; Bourras et al., 2009)—their limited spatio-temporal coverage constrains the  
123 application of the model for global mapping. Buoy-based flux observations provide a  
124 viable alternative. Buoy data offer globally representative flux samples with adequate  
125 volume and acceptable accuracy, which have been widely used to evaluate the  
126 performance of global products (Bentamy et al., 2017; Bourras, 2006; Tang et al., 2024;

127 Weller et al., 2022; Zhou et al., 2020) and support global modeling (Chen et al., 2020a)  
128 and analysis (Song et al., 2024; Yan et al., 2024).

129 The primary objectives of this study are three fold: (1) to develop an innovative  
130 Bowen ratio-constrained statistical model for improving the air-sea SHF, LHF and  $\beta$   
131 estimates (referred to as the BrTHF model hereafter) using the machine learning  
132 technique and global buoy-based air-sea turbulent heat fluxes observations; (2) to  
133 demonstrate the superiority of the statistical model through an inter-comparison with  
134 seven widely used global products and the estimates from the physics-free machine  
135 learning-based model; (3) to produce a global daily  $0.25^\circ$  dataset based on the BrTHF  
136 model over ice-free oceans covering the period from 1993 to 2017. The flux  
137 observations from 197 global distributed buoys, along with multi-source satellite-based  
138 and reanalysis-based inputs, were collected to construct the models and further produce  
139 the global air-sea turbulent heat fluxes dataset. The accuracy and spatio-temporal  
140 patterns of the SHF, LHF and  $\beta$  estimates were inter-compared with seven widely used  
141 products, including the remote sensing-based JOFURO v3, IFREMER v4.1 and  
142 SeaFlux v3, as well as reanalysis-based ERA5 and MERRA2, hybrid-based OAFlux v3  
143 and machine learning-based OHF v2 products.

## 144 **2. Data and Methods**

145 The following sub-sections provide an overview of the development of the BrTHF  
146 product, detailing the construction of air-sea turbulent heat fluxes observation datasets,  
147 learning datasets and the BrTHF model, as well as the evaluation strategies used in this  
148 study, as indicated in Figure 1.



149

150 **Figure 1. flowchart of the generation of a global product of air-sea SHF, LHF and  $\beta$  by the**  
 151 **BrTfH model**

152 **2.1 Air-sea turbulent heat fluxes observation datasets**

153 To obtain the buoy-derived air-sea turbulent heat fluxes observations, the hourly  
 154 or sub-hourly oceanic and atmospheric measurements including sea surface  
 155 temperature ( $T_s$ ), sea surface air temperature ( $T_a$ ), sea surface wind speed ( $WS$ ) and  
 156 relative humidity ( $RH$ ) were firstly collected at 268 buoys covering a variety of ocean  
 157 basins from 13 organizations or networks. Detailed information about the buoy sources  
 158 and the number of buoys from each provider is summarized in Table 1.

159

160 **Table 1 Summary of buoys used in this study**

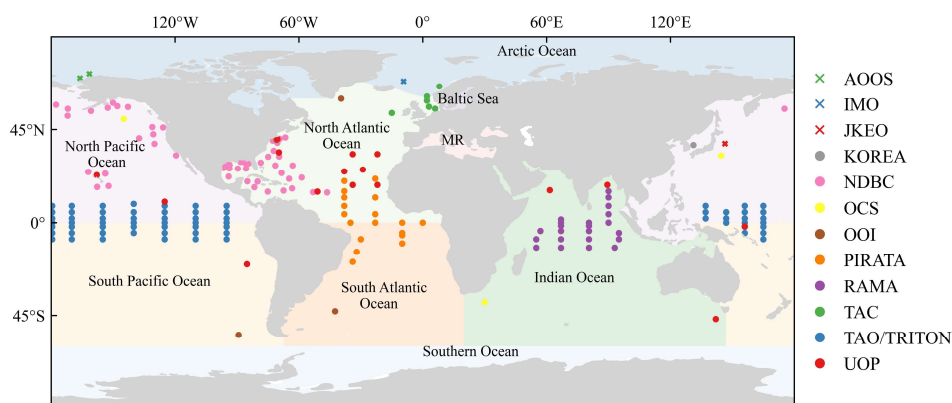
Network/Organization	Number of Buoys	Network/Organization	Number of Buoys
TAO/TRITON (Tropical Atmosphere Ocean / TRITON)	67	KOREA (Korea Meteorological Administration)	24
PIRATA (Prediction and Research Moored Array)	20	OOI (Ocean Observatories Initiative)	6
RAMA (Research Moored Array for Monsoon Analysis)	23	AOOS (Alaska Ocean Observing System)	2
NDBC (National Data Buoy Center)	73	JKEO (Japan Agency for Marine-Earth Science and Tech.)	1
Copernicus Marine In Situ TAC	19	Irish Weather Buoy Network	6
UOP (Upper Ocean Processes Group)	23	Icelandic Meteorological Office (IMO)	1
OCS (Ocean Climate Stations Project)	3		

161 For certain buoys lacking *RH* measurements [e.g. buoys from NDBC (National  
 162 Data Buoy Center) provided dew point temperature (*DEW*) rather than *RH*], the *RH*  
 163 was computed using *DEW* and  $T_a$ . To ensure the quality of the measurements, we  
 164 filtered the records based on the quality control recommendations provided by the data  
 165 providers. Further refinement was also made by removing the questionable values that  
 166 exceeded three standard deviations ( $3\sigma$ ) for each variable at individual buoys.

167 Once the data was cleaned, daily mean aggregation was applied to the oceanic and  
 168 atmospheric measurements. Given the varying temporal resolutions of the  
 169 measurements (e.g. NDBC provided hourly observations before 2005 and 10-min  
 170 observations thereafter), we only retained the daily mean data when the fraction of the  
 171 valid hourly or sub-hourly observations exceeded 80% on a given day.

172 After the above mentioned data preprocessing, the daily buoy-derived air-sea  
 173 turbulent heat fluxes (SHF and LHF) observations were then calculated using the daily  
 174 oceanic and atmospheric measurements combined with the version 3.5 of Coupled  
 175 Ocean-Atmosphere Response Experiment (COARE3.5) model (Edson, 2013)  
 176 (available at <https://zenodo.org/record/5110991>). Although outliers of  $\beta$  exist in  
 177 observations, some are likely caused by measurement errors. Considering that such

178 outliers can severely impede model training and evaluation, it was necessary to  
 179 constrain  $\beta$  within a reasonable range to enable simultaneous high-accuracy estimation  
 180 of SHF, LHF, and  $\beta$ . Therefore, following the air-sea turbulent heat fluxes computations,  
 181 we further made a quality control on the derived SHF and LHF observations to exclude  
 182 the abnormal records, by filtering the observations based on the range of daily  $\beta$  values  
 183 determined from seven widely-used flux products. Specifically, we calculated the  
 184 cumulative distribution of daily  $\beta$  for each product and their ensemble (across all  
 185 products). The medians of the 1<sup>st</sup> and 99<sup>th</sup> percentiles, approximately -5 and 5,  
 186 respectively, were selected as the minimum and maximum of valid daily  $\beta$ , as shown in  
 187 Figure S1. In total, this study compiled 463,585 observations of valid daily air-sea  
 188 turbulent heat flux from 197 buoy stations (Figure 2 and Table S1) in the Arctic Ocean,  
 189 Pacific Ocean, Atlantic Ocean and Indian Ocean.



190  
 191 **Figure 2. Geographic locations of 197 buoy sites from 12 organizations or networks involved**  
 192 **in this analysis including TAO/TRITON, PIRATA, RAMA, NDBC, TAC, UOP, OOI, AOOS,**  
 193 **KOREA, OCS, JKEO and IMO. The boundaries of global land and open oceans were sourced**  
 194 **from the Natural Earth dataset (<https://www.naturalearthdata.com/downloads/>) and the**  
 195 **Global Oceans and Seas dataset (<https://www.marinerregions.org/sources.php>), respectively.**  
 196 **Abbreviations MR refers to the Mediterranean Region. It should be noted that the Caspian**  
 197 **Sea was not included within the boundaries of the open oceans and is shown in white.**

198 Finally, the quality-controlled observations were collected to train and validate the  
 199 BrTHF model. Note that the COARE-based observations at the buoy stations have  
 200 already widely applied as a benchmark for global air-sea turbulent heat flux product

201 development and evaluation (Bentamy et al., 2017; Chen et al., 2020b; Tang et al., 2024;  
202 Weller et al., 2022)

## 203 **2.2 Learning datasets and state-of-the-art products**

### 204 **2.2.1 Learning datasets for training the neural network**

205 Learning variables were carefully selected based on their potential impacts on the  
206 variations of the air-sea turbulent heat fluxes (Grist et al., 2016; Kudryavtsev et al.,  
207 2014; Myslenkov et al., 2021; Song, 2020, 2021; Yan et al., 2024) to conduct the feature  
208 selection (see section 2.3.1). These variables include  $T_a$ , sea surface air specific  
209 humidity ( $Q_a$ ), Mean Sea Level Pressure ( $SLP$ ), Downward Long Wave Radiation Flux  
210 ( $LW$ ), Downward Short Wave Radiation Flux ( $SW$ ),  $T_s$ , sea surface specific humidity  
211 ( $Q_s$ ), Absolute Dynamic Topography ( $ADT$ ), Sea Level Anomaly ( $SLA$ ), Sea Surface  
212 Salinity ( $SSS$ ), Sea Surface Density ( $SSD$ ), Ocean Mixed Layer Current Velocity ( $CS$ ),  
213  $WS$ , Significant Wave Height ( $SWH$ ), Wave period ( $T_p$ ), as well as gradient of  
214 temperature ( $diff_T$ ) calculated using the  $T_s$  and  $T_a$ , and gradient of humidity ( $diff_Q$ )  
215 calculated using the  $Q_s$  and  $Q_a$ .

216 Datasets of these learning variables were collected from multiple publicly  
217 available sources, as summarized in Table 2 and were used as the input features for  
218 training the neural network. The Multi Observation Global Ocean Sea Surface Salinity  
219 and Sea Surface Density (MOGOSD) dataset and Global Ocean Waves (GOW)  
220 Reanalysis dataset were spatially resampled to a  $0.25^\circ$  resolution using mean  
221 aggregation, while temporal mean aggregation to daily values was applied to the GOW  
222 dataset (originally at 3-hour resolution) and Cross-Calibrated Multi-Platform (CCMP)  
223 wind vector analysis dataset (6-hour resolution). Additionally, a daily ERA5 sea-ice  
224 mask was applied to the datasets to mitigate the impact of sea ice.

### 225 **2.2.2 State-of-the-art products for inter-comparison**

226 Seven widely used air-sea turbulent heat fluxes products, involving remote  
227 sensing-based JOFURO3, IFREMER and SeaFlux, as well as reanalysis-based ERA5  
228 and MERRA2, hybrid-based OAFflux and machine learning-based OHF products were

229 selected for inter-comparison.

230 The remote sensing-based JOFURO3, IFREMER, and SeaFlux products were  
231 developed by the Japanese Ocean Flux Data Sets under the Remote Sensing  
232 Observations (J-OFURO) research project, the Institute Français de Recherche pour  
233 l'Exploitation de la Mer (IFREMER), and the NASA Global Hydrology Resource  
234 Center (GHRC) Distributed Active Archive Center (DAAC), respectively. The  
235 reanalysis-based ERA5 and MERRA2 products were developed by the ECMWF and  
236 NASA Global Modeling and Assimilation Office (GMAO), respectively. The hybrid-  
237 based OAFlux and machine learning-based OHF products were developed or published  
238 by the Woods Hole Oceanographic Institution (WHOI) and NOAA Ocean Surface  
239 Bundle (OSB) Climate Data Record (CDR), respectively. With the exception of the  
240 OHF product calculating SHF and LHF simultaneously using a NN model without a  
241 constraint, all other products employed bulk aerodynamic methods to estimate SHF and  
242 LHF. The JOFURO3, IFREMER, and OAFlux products used the COARE3.0 model,  
243 while the SeaFlux used the COARE3.5 model. Differently, the ERA5 adopted the bulk  
244 aerodynamic method used by the ECMWF, and the MERRA2 used the method by the  
245 GEOS. These products provide SHF and LHF estimates at a  $0.25^\circ$  spatial resolution,  
246 except for the MERRA2 ( $0.5^\circ \times 0.625^\circ$ ) and OAFlux ( $1^\circ$ ). Additionally, most products  
247 provide daily SHF and LHF estimates, while only the OHF product provide estimates  
248 at a 3-hour interval. For further inter-comparison, the daily mean aggregation was  
249 applied to the OHF products. More details about the seven products can be found in the  
250 review of Tang et al. (2024).

Table 2 Summary of learning datasets used in this study

Dataset source	Resolution	Variables	Urls
ERA5	0.25°/daily	Sea surface air temperature ( $T_a$ ), sea surface air specific humidity ( $Q_a$ ), mean sea level pressure ( $SLP$ ), downward long wave radiation flux ( $LN$ ) and downward short wave radiation flux ( $SN$ )	<a href="https://cds.climate.copernicus.eu/datasets/derived-era5-single-levels-daily-statistics?tab=overview">https://cds.climate.copernicus.eu/datasets/derived-era5-single-levels-daily-statistics?tab=overview</a>
OSCAR	0.25°/daily	Ocean mixed layer current velocity ( $CS$ )	<a href="https://podaac.jpl.nasa.gov/dataset/OSCAR_L4_OC_FINAL_V2.0">https://podaac.jpl.nasa.gov/dataset/OSCAR_L4_OC_FINAL_V2.0</a>
CCMP	0.25°/6-hour	Wind speed ( $WS$ )	<a href="https://data.remss.com/ccmp/v03.0/daily/">https://data.remss.com/ccmp/v03.0/daily/</a>
MOGOSD	0.125°/daily	Sea surface salinity ( $SSS$ ) and sea surface density ( $SSD$ ),	<a href="https://data.marine.copernicus.eu/product/MULTIOBS_GLO_PHY_S_SURFACE_MYNRT_015_013/description">https://data.marine.copernicus.eu/product/MULTIOBS_GLO_PHY_S_SURFACE_MYNRT_015_013/description</a>
SSH	0.25°/daily	Absolute dynamic topography ( $ADT$ ) and sea level anomaly ( $SLA$ )	<a href="https://data.marine.copernicus.eu/product/SEALEVEL_GLO_PHY_CLIMATE_L4_MY_008_057/description">https://data.marine.copernicus.eu/product/SEALEVEL_GLO_PHY_CLIMATE_L4_MY_008_057/description</a>
GOW	0.2°/3-hour	Significant wave height ( $SWH$ ) and wave period ( $T_p$ )	<a href="https://data.marine.copernicus.eu/product/GLOBAL_MULTITYEAR_WAV_001_032/description">https://data.marine.copernicus.eu/product/GLOBAL_MULTITYEAR_WAV_001_032/description</a>
OISST	0.25°/daily	Sea surface temperature ( $T_s$ ) and sea surface specific humidity ( $Q_s$ )	<a href="https://www.ncei.noaa.gov/data/sea-surface-temperature-optimum-interpolation/v2.1/access/avhrr/">https://www.ncei.noaa.gov/data/sea-surface-temperature-optimum-interpolation/v2.1/access/avhrr/</a>
OISST – ERA5	0.25°/daily	Gradient of temperature ( $diff_T$ ) and gradient of humidity ( $diff_Q$ )	-

253 **Table 3 Summary of the state-of-the-art air-sea turbulent heat fluxes products used for inter-comparison in this study**

Dataset source	Resolution	Model	Variables	Urls
JOFURO3	0.25°/daily	COARE3.0		<a href="https://www.j-ofuro.com/en/">https://www.j-ofuro.com/en/</a>
IFREMER	0.25°/daily	COARE3.0		<a href="ftp://ftp.ifremer.fr/ifremer/cersat/data/heat-flux/ifremer/v4.1/daily">ftp://ftp.ifremer.fr/ifremer/cersat/data/heat-flux/ifremer/v4.1/daily</a>
SeaFlux	0.25°/daily	COARE3.5		<a href="https://www.earthdata.nasa.gov/data/catalog/glnc-daac-seaflux-1">https://www.earthdata.nasa.gov/data/catalog/glnc-daac-seaflux-1</a>
MERRA2	0.5° × 0.625°/daily	GEOS	Latent heat flux (LHF), sensible heat flux (SHF) and Bowen ratio ( $\beta =$ SHF/LHF)	<a href="https://developers.google.com/earth-engine/datasets/catalog/NASA_GSFC_MERRA_flux_2?hl=zh-cn#bands">https://developers.google.com/earth-engine/datasets/catalog/NASA_GSFC_MERRA_flux_2?hl=zh-cn#bands</a>
ERA5	0.25°/daily	ECMWF	Bowen ratio ( $\beta =$ SHF/LHF)	<a href="https://cds.climate.copernicus.eu/datasets/derived-era5-single-levels-daily-statistics?tab=overview">https://cds.climate.copernicus.eu/datasets/derived-era5-single-levels-daily-statistics?tab=overview</a>
OAFflux	1°/daily	COARE3.0		<a href="ftp://ftp.whoi.edu/pub/science/oaf Flux/data_v3">ftp://ftp.whoi.edu/pub/science/oaf Flux/data_v3</a>
OHF	0.25°/3-hour	Neural Network model		<a href="https://www.ncei.noaa.gov/products/climate-data-records/ocean-heat-fluxes">https://www.ncei.noaa.gov/products/climate-data-records/ocean-heat-fluxes</a>

254

## 255 2.3 Construction of the BrTHF model

### 256 2.3.1 Feature selection

257 The study employed a random forest (RF) model to evaluate the importance scores  
258 of 17 oceanic and atmospheric learning variables (with datasets collected in Section 2.2)  
259 for target variables (SHF and LHF), aiming to filter out less influential variables. As  
260 shown in Table S2, the variable importance assessment revealed that  $diff_T$  and  $diff_Q$   
261 showed the highest importance score (71.56% and 49.93%) for SHF and LHF  
262 modelling, respectively; additionally,  $WS$  exhibited the second highest importance for  
263 both SHF (10.19%) and LHF (27.59%) modelling. Building upon the importance  
264 evaluation and through careful screening of highly correlated variables, we ultimately  
265 selected 11 key environmental features for subsequent air-sea turbulent heat fluxes  
266 modelling including  $SLP$ ,  $LW$ ,  $SW$ ,  $SSS$ ,  $ADT$ ,  $CS$ ,  $WS$ ,  $SWH$ ,  $T_p$ ,  $diff_Q$ , and  $diff_T$ .

### 267 2.3.1 Model construction and optimization

268 We selected the NN technique to build the BrTHF model due to its strong ability  
269 to capture the complex nonlinear relationships between the multiple-inputs and  
270 multiple-target variables with high accuracy (Zhou et al., 2024; Fu et al., 2023;  
271 Cummins et al., 2023; Cummins et al., 2024). Additionally, the technique enables the  
272 seamless integration of physical constraints, improving the reasonableness of the results  
273 (Zhou et al., 2024; Zhao et al., 2019; Shang et al., 2023).

274 In order to estimate the SHF and LHF with high accuracy in a physics-consistency  
275 framework, the  $\beta$  (= SHF/LHF) physical constraint was incorporated into the NN model  
276 using the custom multiple-objects (SHF, LHF and  $\beta$ ) loss function as follows:

$$277 \quad LOSS = a \times LOSS_{SHF} + b \times LOSS_{LHF} + c \times LOSS_{\beta} \quad (1)$$

278  $LOSS_{SHF}$ ,  $LOSS_{LHF}$  and  $LOSS_{\beta}$  represent the Mean Squared Error (MSE) of SHF, LHF and  
279  $\beta$ , respectively. They were weighted using the factors of  $a$  (SHF),  $b$  (LHF) and  $c$  ( $\beta$ ) to  
280 balance the different magnitudes of loss during optimization. To prevent potential  
281 gradient explosion during model training, predicted  $\beta$  [ $SHF'/LHF'$ , calculated using the  
282 predicted SHF ( $SHF'$ ) and LHF ( $LHF'$ )] values were clipped within the observed range

283 of  $\beta$  (from -5 to 5) during training:

$$284 \quad CLIP\left(\frac{SHF'}{LHF'}\right) = \begin{cases} \text{Min}\left(\frac{SHF'}{LHF'}, 5\right) & \frac{SHF'}{LHF'} > 0 \\ \text{Max}\left(\frac{SHF'}{LHF'}, -5\right) & \frac{SHF'}{LHF'} < 0 \end{cases} \quad (2)$$

$$285 \quad Loss_{\beta} = MSE\left(\frac{SHF'}{LHF'}, CLIP\left(\frac{SHF'}{LHF'}\right)\right) \quad (3)$$

286 Finally, after optimization, the final weights (a, b and c) for SHF, LHF, and  $\beta$  were  
287 set to 5, 1, and 250, respectively. The model was constructed consisting of one input  
288 layer, three hidden layers, two BatchNormalization layers, and one output layer using  
289 the Python TensorFlow library. The number of neurons in the three hidden layers were  
290 32, 64, and 16, respectively and the activation function of Leaky Rectified linear unit  
291 (ReLU) was used throughout the model.

292 To illustrate the superiority of the BrTHF model in terms of accuracy and physical  
293 consistency, another physics-free NN models, trained without integrating the  $\beta$   
294 constraint, were also constructed to predict SHF and LHF separately for further  
295 comparison, where  $\beta$  was calculated to be SHF/LHF.

## 296 **2.4 Evaluation strategy**

297 A spatial 10-fold cross-validation was employed to assess the performances of the  
298 BrTHF model for estimating air-sea SHF, LHF and  $\beta$ . Compared to the traditional 10-  
299 fold cross-validation, which randomly split all samples into ten folds and thus may  
300 result in overlapping spatial samples between training and validating datasets, the  
301 spatial 10-fold cross-validation were conducted in a relatively independent spatial  
302 distribution and can provide a more generalized and convincing evaluation.

303 Specifically, first, all buoy sites were randomly split into ten folds. Then, each fold  
304 was in succession selected as the validation dataset and the rest of ten folds was used  
305 as the training dataset.

306 The metrics used to evaluate the performance of the models include: (1) the mean  
307 bias error (BIAS); (2) the root mean squared error (RMSE); (3) the correlation  
308 coefficient (r):

309 
$$BIAS = \frac{1}{n} \sum_{i=1}^n (\hat{y}_i - y_i) \quad (4)$$

310 
$$RMSE = \sqrt{\frac{1}{n} \sum_{i=1}^n (\hat{y}_i - y_i)^2} \quad (5)$$

311 
$$r = \frac{\sum_{i=1}^n [(\hat{y}_i - \bar{\hat{y}})(y_i - \bar{y})]}{\sqrt{\sum_{i=1}^n (\hat{y}_i - \bar{\hat{y}})^2 \sum_{i=1}^n (y_i - \bar{y})^2}} \quad (6)$$

312 where  $n$  is the number of samples,  $\hat{y}_i$  and  $y_i$  are the estimated value and reference  
 313 truth,  $\bar{\hat{y}}$  and  $\bar{y}$  are the mean of  $\hat{y}_i$  and  $y_i$ , respectively. These metrics—BIAS,  
 314 RMSE, and  $r$ —comprehensively evaluate model performance, representing systematic  
 315 deviation, dispersion between observations and estimates, and the strength and  
 316 direction of the linear relationship, respectively.

317

### 318 **3. Results and discussion**

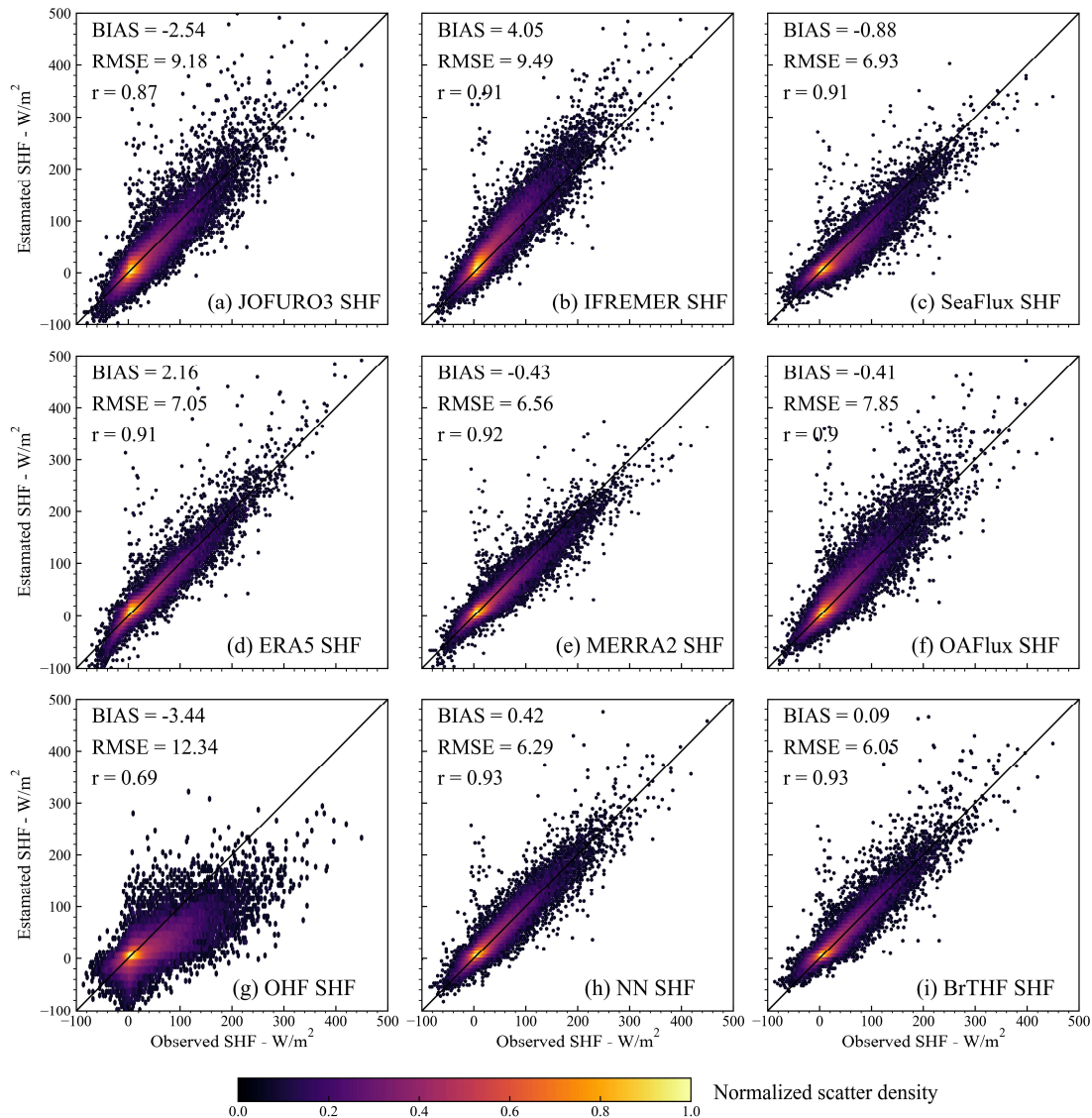
#### 319 **3.1 Spatial ten-fold cross-validation of the models**

##### 320 **3.1.1 Overall accuracy**

321 Figures 3, 4 and 5 present the normalized scatter density plots of the estimated  
 322 daily SHF, LHF and  $\beta$  from the BrTHF and physics-free NN models, as well as the  
 323 seven air-sea turbulent heat fluxes products against the observations obtained from 197  
 324 global distributed buoys by the spatial ten-fold cross-validation strategy.

325 Most models and products showed data distributions closely aligned with the  
 326 observed SHF, with the majority of samples clustered around the 1:1 line. The BrTHF  
 327 model slightly overestimated SHF with a BIAS of 0.09 W/m<sup>2</sup>, whereas the physics-free  
 328 NN models, ERA5 and IFREMER products showed more pronounced overestimations  
 329 (from 0.42 W/m<sup>2</sup> to 4.05 W/m<sup>2</sup>). In contrast, the rest five products exhibited notable  
 330 underestimations (from -3.44 W/m<sup>2</sup> to -0.41 W/m<sup>2</sup>). As illustrated in Figure 6, the  
 331 variability of estimated SHF from the BrTHF and the physics-free NN models and  
 332 ERA5 product closely matched the observed SHF, all with a Standard Deviation (STD)  
 333 of approximately 16 W/m<sup>2</sup>. Notably, the BrTHF model achieved the lowest RMSE  
 334 (6.05 W/m<sup>2</sup>), outperforming both the physics-free NN models (6.29 W/m<sup>2</sup>) and the

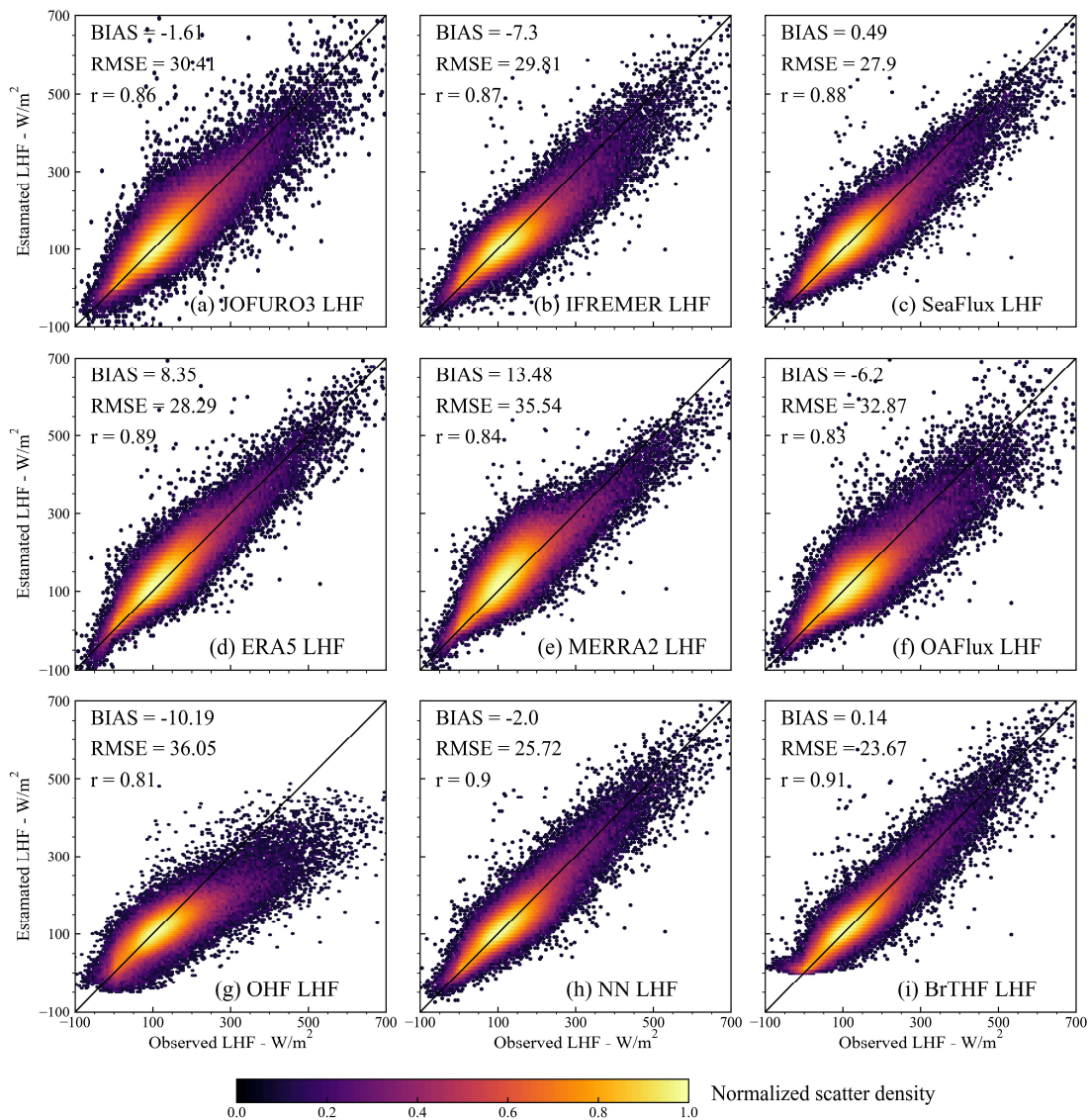
335 seven air-sea turbulent heat flux products (ranging up to 12.34  $\text{W}/\text{m}^2$  for OHF).  
 336 Additionally, the BrTHF model combined with the physics-free NN models yielded the  
 337 highest values of  $r$  (0.93), surpassing all seven other products. In summary, the BrTHF  
 338 model showed overall the best performance in estimating SHF among all the models  
 339 and products.



340  
 341 **Figure 3. Normalized scatter density plots of estimated SHF from the BrTHF model, the**  
 342 **physics-free NN models and seven air-sea turbulent heat fluxes products against the observed**  
 343 **SHF obtained from 197 global distributed buoys.**

344 For LHF, similar to the results for SHF, the BrTHF model also demonstrated the  
 345 best agreement with observations, achieving the lowest RMSE ( $23.67 \text{ W}/\text{m}^2$ ) and the

346 highest value of  $r$  (0.91). Compared to the physics-free NN models and seven products,  
 347 the BrTHF model reduced RMSE by  $2.05 \text{ W/m}^2$  (physics-free NN models) to  $12.38$   
 348  $\text{W/m}^2$  (OHF) and improved  $r$  by  $0.01$  (physics-free NN model) to  $0.1$  (OHF).  
 349 Additionally, the BrTHF model showed a slight overestimation of LHF (BIAS =  $0.14$   
 350  $\text{W/m}^2$ ), lower than that of the SeaFlux, MERRA2, and ERA5 products. In contrast, the  
 351 remaining products (JOFURO3, IFREMER, OAFflux, and OHF), along with the  
 352 physics-free NN models, underestimated LHF, with the BIAS values ranging from -  
 353  $10.19 \text{ W/m}^2$  (OHF) to  $-1.61 \text{ W/m}^2$  (JOFURO3).



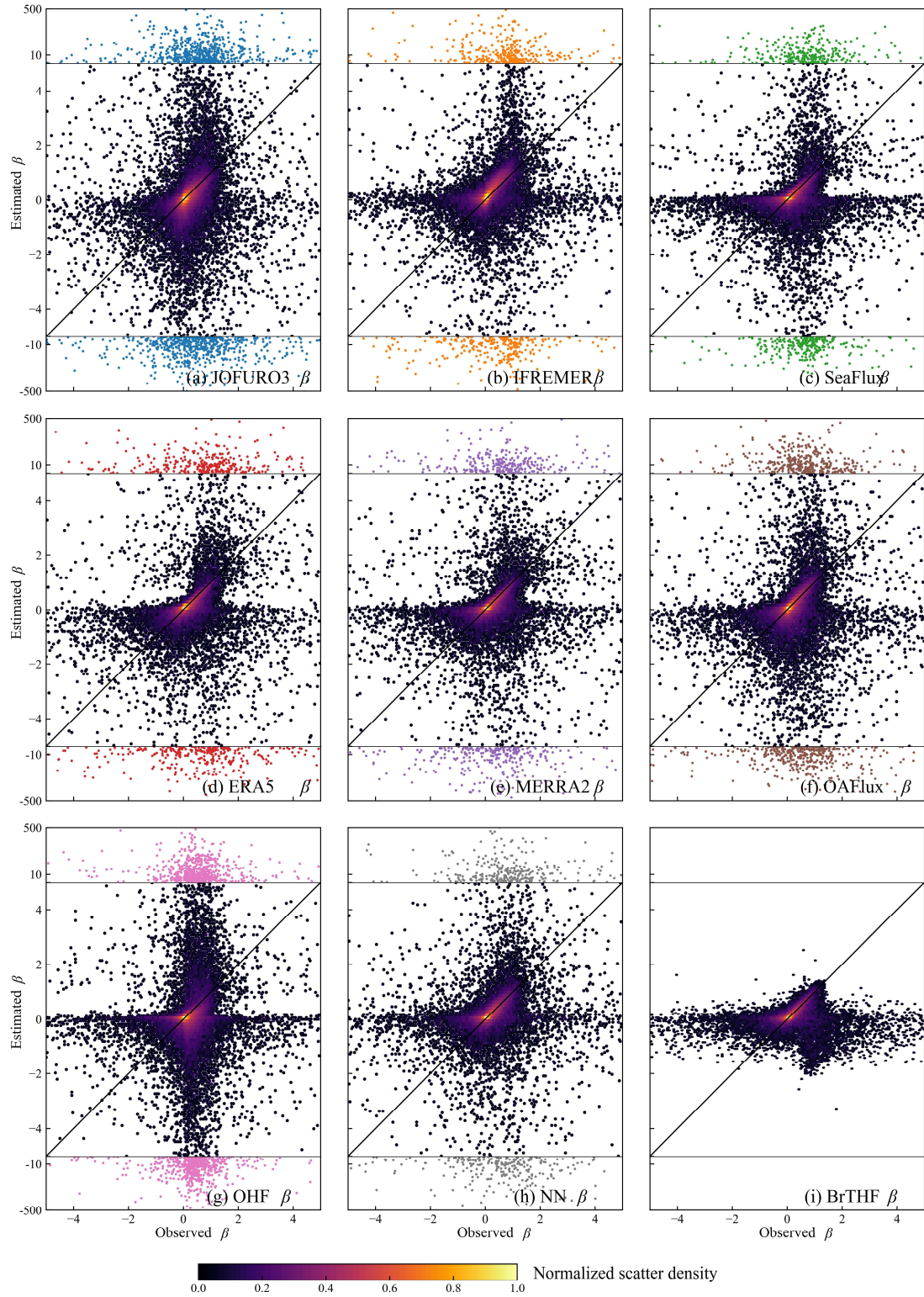
354

355 **Figure 4. Same as Figure 3 but for LHF.**

356

The BrTHF model exhibited a significantly different distribution of  $\beta$  compared to

357 the physics-free NN models and the seven products, as shown in Figure 5. The  $\beta$   
358 estimates from the BrTHF model consistently fell within the observed range of -5 to 5,  
359 while the physics-free NN model and the seven products occasionally produced  
360 estimates outside this range. Specifically, approximately 0.9% of  $\beta$  estimates from both  
361 the physics-free NN model and the seven products were out of range. The extreme  
362 positive and negative  $\beta$  estimates were found in the OHF ( $\beta = 14997$ ) and physics-free  
363 NN models ( $\beta = -25703$ ) products, respectively. The abnormal  $\beta$  estimates significantly  
364 impacted the accuracy of the physics-free NN models and the seven products as Figure  
365 6 indicated. When excluding the abnormal  $\beta$  samples from the physics-free NN models  
366 and seven products, the RMSEs ranged from 0.17 (physics-free NN models and  
367 SeaFlux) and 0.26 (OHF), with values of  $r$  ranging from 0.13 (OHF) to 0.46  
368 (IFREMER), as shown in Figure 6 and Table S3. However, when all estimates were  
369 considered, the performances of these model and products deteriorated sharply, with  
370 RMSEs rising from 0.87 (SeaFlux) to 39.21 (physics-free NN models), and values of  $r$   
371 dropping from 0.06 (SeaFlux) to 0 (JOFURO3, MERRA2 and OHF). In contrast, the  
372 BrTHF model maintained robust outperformance, with the lowest RMSEs of 0.22 and  
373 0.15, and higher  $r$  values of 0.25 and 0.43, both before and after removing the abnormal  
374  $\beta$  samples from the physics-free NN models and the seven products. Notably, the BIAS  
375 values remained stable (ranging from -0.04 to 0.04) for all models and products,  
376 regardless of whether the abnormal samples were excluded.



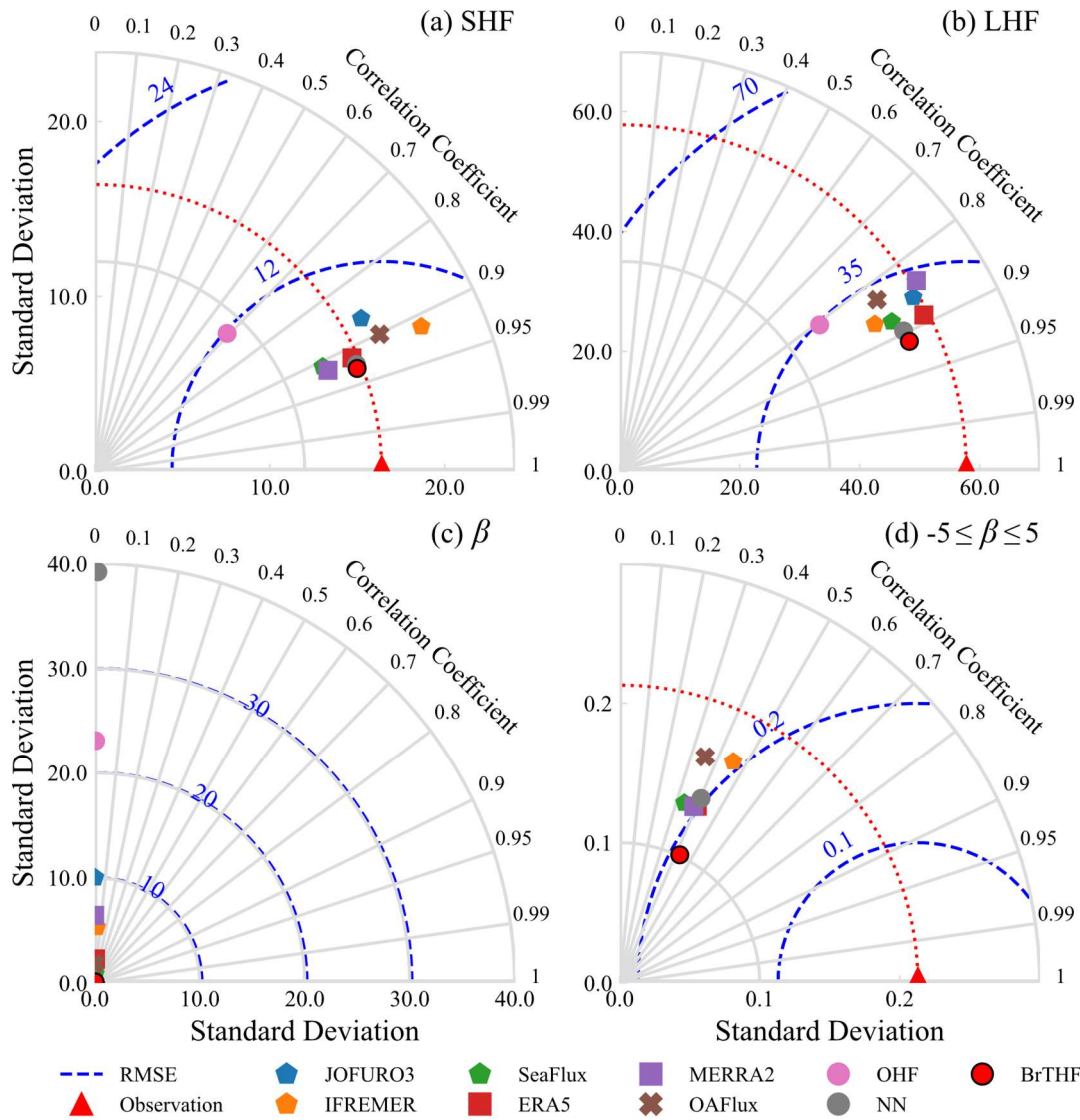
377

378 **Figure 5. Same as Figure 3 but for  $\beta$ . The samples out of the ranges of observed  $\beta$  ( $-5 \leq \beta \leq 5$ )**

379 **were colored in blue, orange, green, red, purple, brown, pink and gray for JOFURO3,**

380 **IFREMER, SeaFlux, ERA5, MERRA2, OAFflux, OHF products and the physics-free NN**

381 **models, respectively. The statistical metrics could be found in Table S3 and Figure 6.**



382

383 **Figure 6. Taylor diagrams of the validation of estimated daily SHF (a), LHF (b),  $\beta$  (c) and  $\beta$  ( $-5 \leq \beta \leq 5$ , d) from the BrTHF model, the physics-free NN models and the seven products against the in-situ observations.**

386

### 387 3.1.2 Accuracies across oceans

388 To better understand the accuracy of SHF, LHF and  $\beta$  estimates from the BrTHF  
 389 and physics-free NN models, as well as the seven products in different oceans, we  
 390 conducted an additional evaluation by categorizing the observations according to the  
 391 belonging ocean basins, as shown in Figure 7. The major ocean boundaries, obtained  
 392 from Marine Regions (<https://www.marineregions.org/>), were used to define the ocean

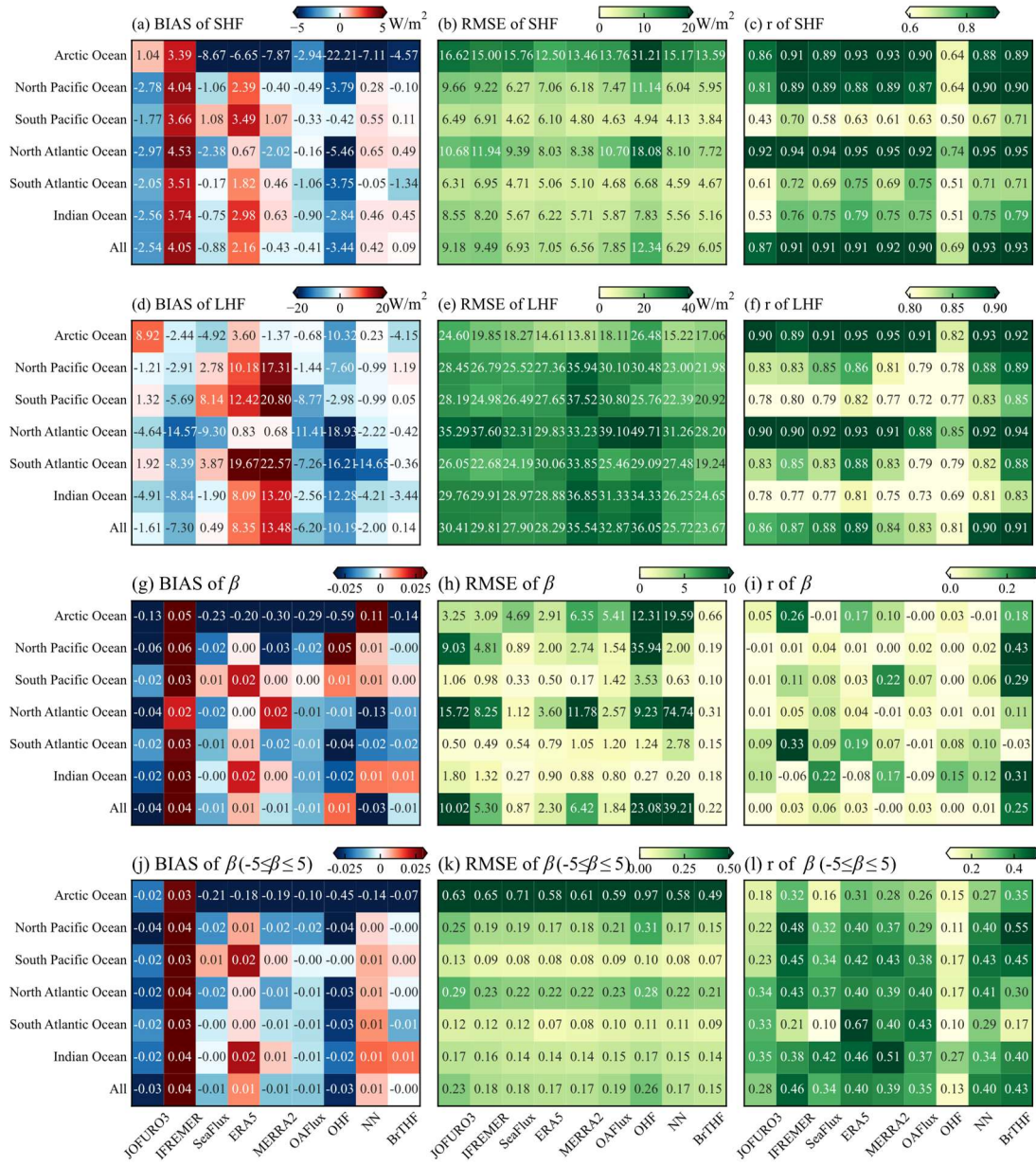
393 basins, which include the Arctic Ocean, South Pacific Ocean, North Pacific Ocean,  
394 South Atlantic Ocean, North Atlantic Ocean, and Indian Ocean.

395 For SHF, the BrTHF model exhibited overestimations in the South Pacific Ocean,  
396 North Atlantic Ocean, and Indian Ocean, while it underestimated SHF in the remaining  
397 three ocean basins. The values of BIAS ranged from  $-4.57 \text{ W/m}^2$  in the Arctic Ocean to  
398  $0.49 \text{ W/m}^2$  in the North Atlantic Ocean. Furthermore, the BrTHF achieved the lowest  
399 RMSEs in most ocean basins, ranging from  $3.84 \text{ W/m}^2$  in the South Atlantic Ocean to  
400  $7.72 \text{ W/m}^2$  in the North Atlantic Ocean, except in the Arctic Ocean where the RMSE of  
401  $13.59 \text{ W/m}^2$  were higher than those of the ERA5 ( $12.5 \text{ W/m}^2$ ) and MERRA2 ( $13.46$   
402  $\text{W/m}^2$ ) products, as shown in Figure 7(b). Correlation analysis also demonstrated the  
403 robust performance of the BrTHF model in estimating SHF, with values of  $r$  exceeding  
404  $0.89$  in most ocean basins, except those ocean basins in the South Hemisphere (ranging  
405 from  $0.71$  to  $0.79$ ) where the values of  $r$  for all models and products reduced.

406 For LHF, the values of BIAS of the BrTHF model ranged from  $-4.15 \text{ W/m}^2$  in the  
407 Arctic Ocean to  $1.19 \text{ W/m}^2$  in the North Pacific Ocean. In comparison, the BrTHF  
408 model showed more pronounced underestimations in the Arctic Ocean and Indian  
409 Ocean. Additionally, the BrTHF model outperformed the physics-free NN models and  
410 the seven products across most ocean basins, achieving the lowest RMSEs (ranging  
411 from  $17.06 \text{ W/m}^2$  in the Arctic Ocean to  $28.20 \text{ W/m}^2$  in the North Atlantic Ocean) and  
412 the highest values of  $r$  (ranging from  $0.83$  in the Indian Ocean to  $0.94$  in the North  
413 Atlantic Ocean) except for the Arctic Ocean where the value of  $r$  was  $0.01$  less than the  
414 physics-free NN models and the RMSE were  $2.45 \text{ W/m}^2$ ,  $3.25 \text{ W/m}^2$  and  $1.84 \text{ W/m}^2$   
415 higher than the ERA5 and MERRA2 products and the physics-free NN models,  
416 respectively.

417 The BrTHF model consistently performed better in estimating  $\beta$  across most ocean  
418 basins, both before and after removing the abnormal  $\beta$  samples that deviated from the  
419 observed range ( $-5 \leq \beta \leq 5$ ). In contrast, the physics-free NN models and the seven  
420 products did not perform as well. Specifically, the BrTHF model exhibited the lowest

421 RMSEs in almost all ocean basins except in the South Atlantic Ocean after removing  $\beta$   
 422 outliers. Moreover, in terms of correlation analysis, the BrTHF model achieved higher  
 423 values of  $r$  in most ocean basins before and after the removal of abnormal  $\beta$  samples,  
 424 among all models and products.

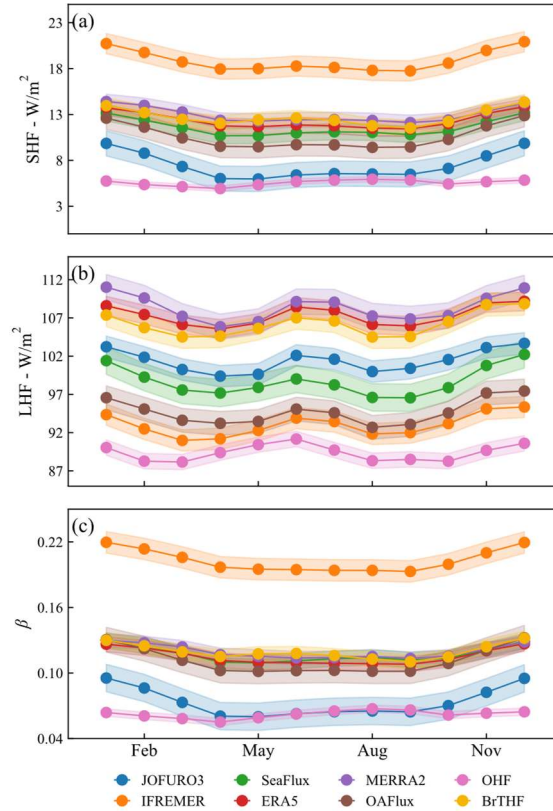


425  
 426 **Figure 7. Heatmaps of BIAS, RMSE and  $r$  metrics for the validation of estimated daily SHF**  
 427 **(a - c), LHF (b - e),  $\beta$  (f - i) and  $\beta$  ( $-5 \leq \beta \leq 5$ , j - l) from the BrTHF model, the physics-free NN**  
 428 **models and the seven products against the in-situ observations across different ocean basins.**  
 429 **It should be noted that the statistical metrics for each ocean basin were calculated using**  
 430 **observations from the available buoys within the corresponding basin.**

### 431 **3.2 Temporal variations in SHF, LHF and $\beta$**

432 After spatial ten-fold cross-validation, we produced the daily  $0.25^\circ$  global air-sea  
433 turbulent heat fluxes products from 1993 to 2017 using a combination of the BrTHF  
434 model and learning datasets, and further made a comparison of the temporal variation  
435 (in this section), spatial distribution (in Section 3.3) and annual trend (in Section 3.4)  
436 of SHF, LHF and  $\beta$  estimates from the BrTHF product and those with the seven state-  
437 of-the-art global products. The selected period (from 1993 to 2017) was determined by  
438 the overlapping availability of input learning datasets.

439 Figure 8 illustrates the monthly area-weighted global means of SHF, LHF and  $\beta$   
440 from 1993 to 2017 for the BrTHF product and seven state-of-the-art products. The  
441 BrTHF product exhibited similar bimodal patterns for SHF, LHF and  $\beta$  as the seven  
442 products, with peaks in December-January and May-June-July-August. In addition, the  
443 peak in May-June-July-August was less pronounced for SHF and  $\beta$  compared to that  
444 for LHF. The monthly area-weighted global means of SHF and  $\beta$  from the BrTHF  
445 product were higher than those of most products, except for the MERRA2 product in  
446 January, February, March, April, July, August and September, and the IFREMER  
447 product in all months. For LHF, the BrTHF showed lower values than the ERA5 and  
448 MERRA2 products across all months. Notably, the patterns of SHF and  $\beta$  from the OHF  
449 product, with the highest peak occurring in August and smoother intra-annual cycles,  
450 differed from those of the corresponding BrTHF product and the other six products  
451 developed using the bulk aerodynamic methods.

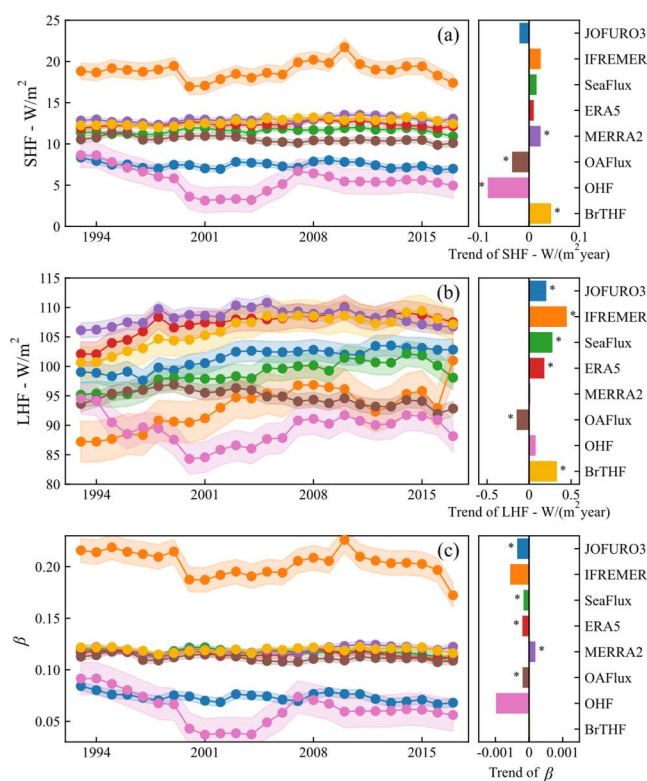


452

453 **Figure 8. Intra-annual cycles of area-weighted global monthly mean of SHF (a), LHF (b) and**  
 454  **$\beta$  (c) from the eight products from 1993 to 2017. The shaded areas indicate  $\pm 1$  standard**  
 455 **deviation around the mean.**

456 Figure 9 presents the temporal evolution of the area-weighted annual global mean  
 457 of SHF, LHF and  $\beta$  from 1993 to 2017 for the eight products for the ice-free oceans.  
 458 The global mean annual SHF of the BrTHF product was  $12.7 \text{ W/m}^2$ , which was close  
 459 to those of SeaFlux ( $11.6 \text{ W/m}^2$ ), OAFflux ( $10.6 \text{ W/m}^2$ ), MERRA2 ( $13 \text{ W/m}^2$ ) and  
 460 ERA5 ( $12.4 \text{ W/m}^2$ ), whereas significantly lower than that of IFREMER ( $18.8 \text{ W/m}^2$ )  
 461 and higher than those of JOFURO3 ( $7.5 \text{ W/m}^2$ ) and OHF ( $5.6 \text{ W/m}^2$ ). Meanwhile, the  
 462 BrTHF product exhibited significant largest growth of SHF with the trend of  $0.04$   
 463  $\text{W}/(\text{m}^2 \cdot \text{year})$  among all eight products, and showed similar temporal evolution as  
 464 SeaFlux, MERRA2, ERA5 and OAFflux during the period from 1993 to 2017. As for  
 465 LHF, the BrTHF exhibited a larger global mean annual value of  $106.2 \text{ W/m}^2$ , which  
 466 was close to those of the ERA5 ( $107.3 \text{ W/m}^2$ ) and MERRA2 ( $108.3 \text{ W/m}^2$ ), and it was  
 467 significantly higher than rest of the products. Moreover, the growth of the BrTHF LHF

468 was significant with a trend of  $0.33 \text{ W}/(\text{m}^2 \cdot \text{year})$ , which was lower than the IFREMER  
 469 but higher than the OAFlux, MERRA2, OHF, ERA5, JOFURO3 and SeaFlux, ranging  
 470 from  $-0.14 \text{ W}/(\text{m}^2 \cdot \text{year})$  to  $0.4 \text{ W}/(\text{m}^2 \cdot \text{year})$ . Note that only the OAFlux product showed  
 471 negative trend of LHF from 1993 to 2017. For  $\beta$ , the BrTHF showed a similar temporal  
 472 pattern to that of SHF, and most products concentrated within the narrow range of 0.11  
 473 to 0.12 for the annual values. The magnitude of annual  $\beta$  of the BrTHF was about 0.11,  
 474 which was close to the OAFlux, SeaFlux, MERRA2 and ERA5, but significantly lower  
 475 than the IFREMER and higher than the JOFURO3 and OHF. Moreover, in contrast to  
 476 the significant increasing trends of LHF and SHF, negative of trends of  $\beta$  were shown  
 477 for most products. However, the BrTHF product exhibited a weak positive trend, which  
 478 may be attributed to the relatively smaller differences between the SHF and LHF trends  
 479 in BrTHF compared to those in other products.

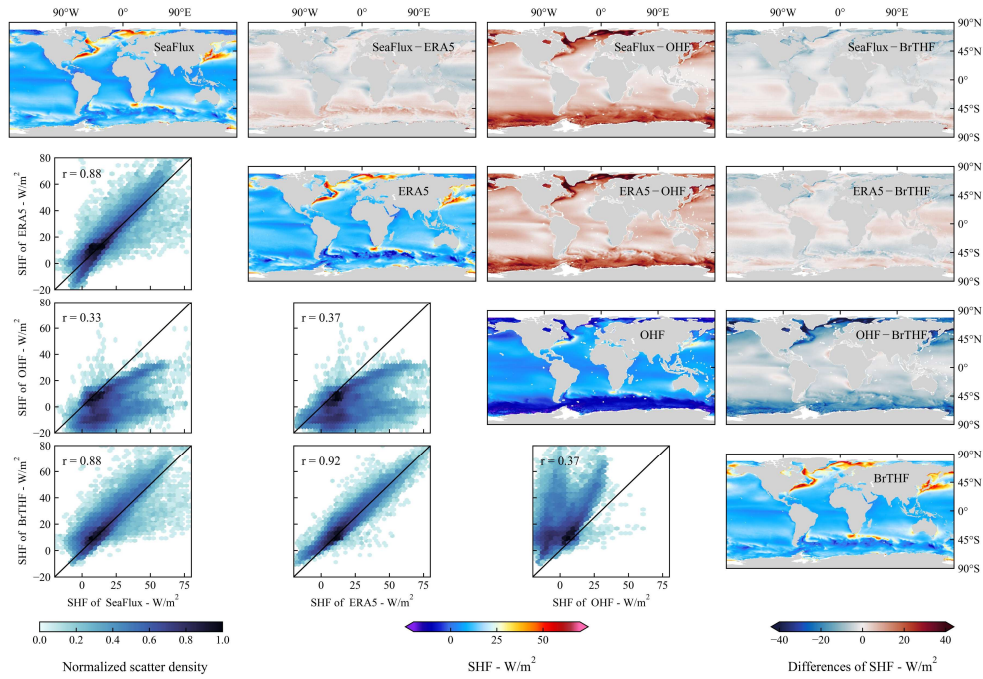


480  
 481 **Figure 9. Inter-annual evolution of area-weighted global mean SHF (a - b), LHF (c - d) and  $\beta$**   
 482 **(e - f) from 1993 to 2017. The trends were calculated based on the Sen's slope method. The \***  
 483 **in the sub-figures (b, d and f) represent the trend passed the Mann-Kendall significant test ( $p$**   
 484  **$< 0.05$ ). The shaded areas indicate  $\pm 1$  standard deviation around the mean.**

### 485 3.3 Inter-comparison of the spatial pattern

486 We selected three representative products including the (reanalysis-based) ERA5,  
487 (remote sensing-based) SeaFlux, and (the only publicly available machine learning-  
488 based) OHF products to evaluate the BrTHF product's ability in simulating global air-  
489 sea turbulent heat fluxes (SHF, LHF, and  $\beta$ ) from 1993 to 2017. These products were  
490 chosen because they demonstrated relatively high accuracy within their respective  
491 categories (as shown in Section 3.1) and shared the same  $0.25^\circ$  spatial resolution with  
492 the BrTHF product.

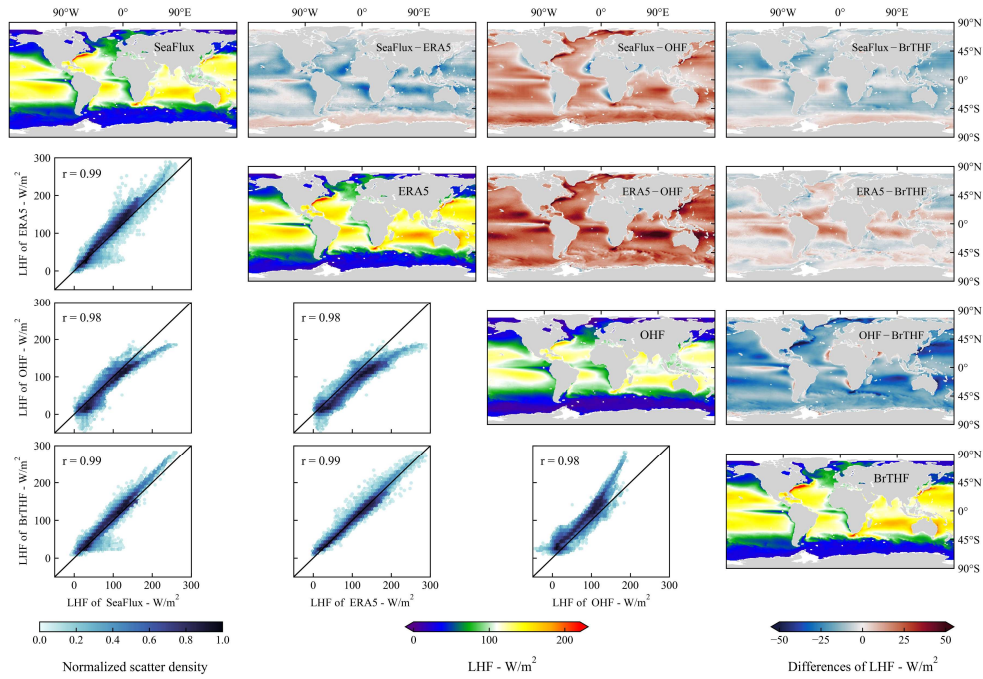
493 Figure 10 presents the spatial distribution of multi-year mean of SHF from the  
494 SeaFlux, ERA5, BrTHF, and OHF products, along with their cross-comparisons.  
495 Overall, the BrTHF product exhibited strong consistency with ERA5 and SeaFlux  
496 products, with values of  $r$  exceeding 0.88, which was significantly higher than the  
497 consistency between SeaFlux and OHF ( $r = 0.33$ ) and between ERA5 and OHF ( $r =$   
498  $0.37$ ). Spatially, the BrTHF, SeaFlux and ERA5 products all showed higher SHF (over  
499  $50 \text{ W/m}^2$ ) in the Western Boundary Currents (WBCs, e.g. Kuroshio, Gulf Stream, Brazil  
500 Current and Agulhas Current) regions, whereas OHF product yielded much lower SHF  
501 ( $\sim 25 \text{ W/m}^2$ ). Additionally, the former three products captured pronounced SHF  
502 gradients in the Southern Ocean, features that were absent in OHF product. SHF  
503 differences between BrTHF and SeaFlux/ERA5 remained within  $\pm 10 \text{ W/m}^2$  in most  
504 oceans. The BrTHF product exhibited slightly higher SHF values than SeaFlux in the  
505 Northern Hemisphere, whereas in the Southern Hemisphere—particularly over the  
506 Southern Ocean—the BrTHF showed relatively lower SHF. Compared to the ERA5  
507 product, the BrTHF product yielded lower SHF in the equatorial zone, subtropical high-  
508 pressure regions and the Southern Ocean, but higher SHF in other areas, particularly in  
509 the North Pacific and the southern Indian Ocean.



510

511 **Figure 10. Inter-comparison of the spatial distributions of multi-year means of SHF among**  
 512 **the SeaFlux, ERA5, OHF and BrTHF products from 1993 to 2017.**

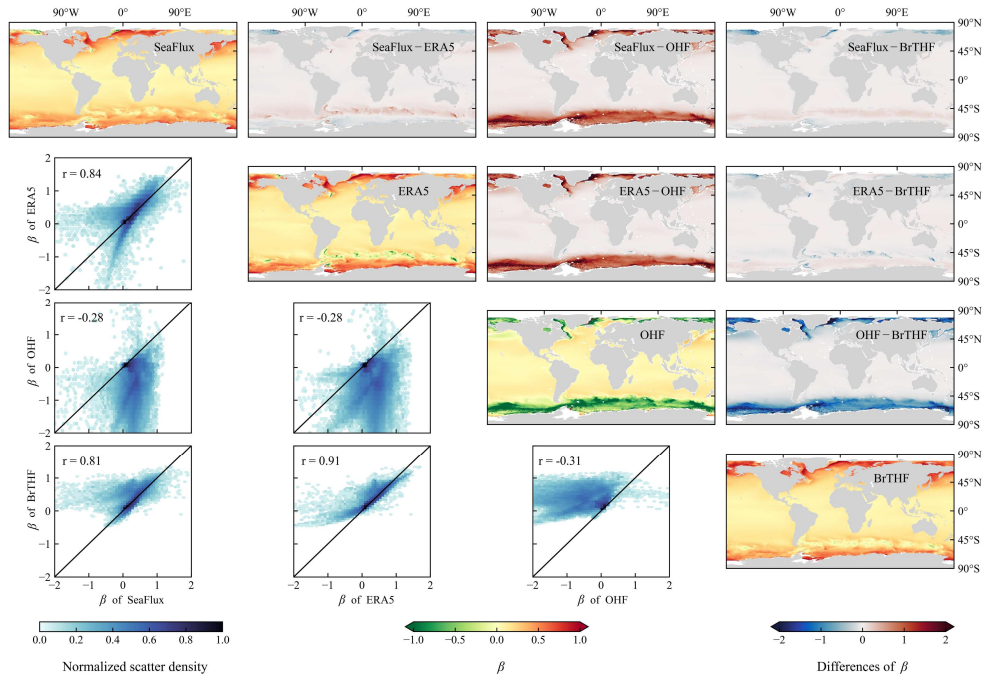
513 For LHF, the BrTHF and the selected three products exhibited more close spatial  
 514 distribution patterns, with the values of  $r$  exceeding 0.98, compared to the results for  
 515 the SHF, as shown in Figure 11. The higher LHF (over  $150 \text{ W/m}^2$ ) primarily occurred  
 516 around the regions of WBCs and the sub-tropic highs, while lower LHF (below  $50$   
 517  $\text{W/m}^2$ ) appeared in the Eastern Equatorial Pacific and Atlantic Warm Tongue and the  
 518 oceans with latitudes higher than  $45^\circ$ . The spatial distribution of LHF in the BrTHF  
 519 product generally agreed better with that of the ERA5 product, though the BrTHF  
 520 showed significantly lower LHF in sub-tropic highs. Additionally, the BrTHF exhibited  
 521 relatively lower LHF than the ERA5 over the Southern Ocean and the central North  
 522 Atlantic. Compared to the SeaFlux, the BrTHF yielded slightly higher LHF in most  
 523 oceans except the Southern Ocean and equatorial zones.



524

525 **Figure 11. Same as Figure 10 but for LHF.**

526 For  $\beta$ , the BrTHF product demonstrated strong spatial correlation with the ERA5  
 527 and SeaFlux in multi-year mean distributions, with values of  $r$  exceeding 0.81. In  
 528 contrast, the OHF showed markedly a different spatial pattern of  $\beta$ , exhibiting negative  
 529 correlations when compared to the rest of three products. Spatially, the BrTHF product's  
 530  $\beta$  distribution aligned more closely with the SeaFlux, both displaying higher  $\beta$  (up to 1)  
 531 in high-latitude oceans particularly in the Northern Hemisphere and the similar  
 532 wavelike textures of  $\beta$  over the Southern Ocean's Antarctic Circumpolar Current zone.  
 533 The differences between the BrTHF and OHF products were more evident. Specifically,  
 534 the BrTHF product showed overall overestimation of  $\beta$  in the oceans where latitudes  
 535 were larger than  $45^\circ$  compared to the OHF product.



536

537 **Figure 12. Same as Figure 10 but for  $\beta$ .**

538

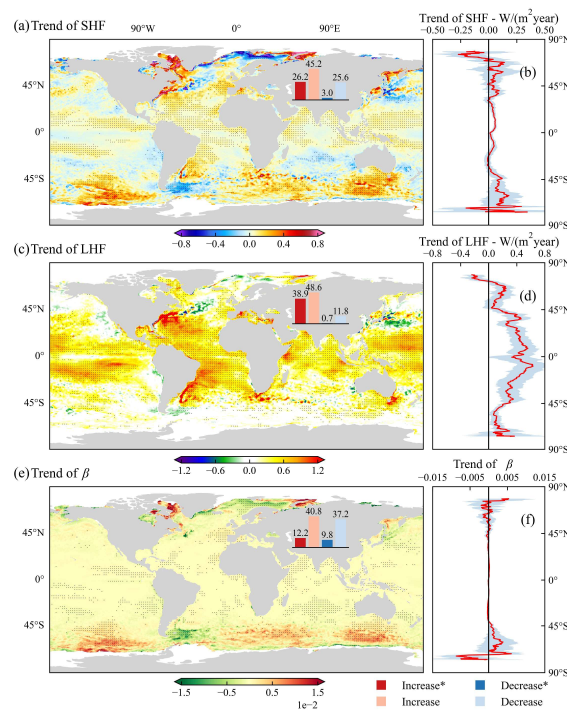
### 539 3.4 Spatial pattern of trends in SHF, LHF and $\beta$ from the BrTHF product

540 Figure 13 illustrates the spatial distribution of inter-annual trends of SHF, LHF and  
 541  $\beta$  in the BrTHF product from 1993 to 2017. The SHF showed increasing trends across  
 542 71.4% of the oceans, with statistically significant increases in 26.2% of regions. In  
 543 contrast, decreasing trends were observed in 28.6% of the oceans, with only 3%  
 544 showing significant reductions. Overall, the trends of zonal annual averages of SHF  
 545 remained stable between the 60°N to 45°S, with significant increases occurring  
 546 southward and decreases northward. Specifically, moderate increases ( $\sim 0.2$  W/(m<sup>2</sup>  
 547 year)) dominated between 45°N and 45°S, while more pronounced increases ( $> 0.8$   
 548 W/(m<sup>2</sup> year)) were observed in high-latitude oceans, including the Kara Sea, Gulf  
 549 Stream, Baffin Bay, Brazil Current, Sea of Okhotsk, and Sea of Japan. Notable  
 550 decreases ( $< -0.8$  W/(m<sup>2</sup> year)) were concentrated in the Barents Sea and the central  
 551 North Atlantic.

552 The LHF exhibited markedly different characteristics of the spatial distribution,  
 553 with 87.5% of oceans showing increasing trends (38.9% were significant), versus 12.5%  
 554 decreasing (0.7% were significant). In contrast to those of the SHF, the trends of zonal

555 annual averages for LHF weakened poleward from the oceans of Equator. The  
 556 substantial increases ( $>0.6 \text{ W/m}^2/\text{year}$ ) occurred in the oceans between  $45^\circ\text{N}$  to  $45^\circ\text{S}$ ,  
 557 particularly in the Gulf Stream, Brazil Current, and Agulhas Current systems, while  
 558 notable decreases (lower than  $-0.3 \text{ W/m}^2/\text{year}$ ) were observed in the central North  
 559 Atlantic and Kuroshio extension regions.

560 For  $\beta$ , approximately 53% of the oceans showed increasing trends, with 12.2% of  
 561 these being statistically significant. Conversely, about 47% of the oceans showed  
 562 decreasing trends, with 9.8% being significant. Most oceans between  $45^\circ\text{N}$  to  $45^\circ\text{S}$   
 563 exhibited near-zero trends, while significant trends were concentrated in the high-  
 564 latitude oceans. Notable increases were found in Baffin Bay, Kara Sea, and the Southern  
 565 Ocean, while decreases were observed in the Barents Sea and the Southern Ocean near  
 566 South America.



567 **Figure 13. Spatial maps of inter-annual trends for SHF (a), LHF (c), and  $\beta$  (e) from the BrTHF**  
 568 **product for the period 1993 to 2017. The trends were calculated using the Sen’s slope method.**  
 569 **Dotted areas indicate oceans where the p-value of the Mann-Kendall significance test is less**  
 570 **than 0.05. Panels (b), (d) and (f) represent the inter-annual trends of zonal annual averages**  
 571 **for SHF, LHF and  $\beta$ , respectively.**  
 572

### 573 3.5 Discussion

574 Advancing our understanding of the air-sea interaction and achieving the global  
575 closure of the ocean surface energy budget require accurate global-scale simulations of  
576 air-sea turbulent heat fluxes (Yu, 2019). Existing global air-sea turbulent heat fluxes  
577 products, primarily generated using the semi-empirical bulk aerodynamic methods and  
578 data-driven machine learning approach, are often weak in accuracy and physical  
579 rationality, arising from uncertainties in environmental forcings and inappropriate  
580 parameterizations (Brodeau et al., 2017; Jiang et al., 2024a; Wang et al., 2024). To  
581 improve the simulation of the global air-sea turbulent heat fluxes, this study presents  
582 the BrTHF product, generated using a Bowen ratio-constrained NN technique with a  
583 custom multiple-objective loss function, as well as observations from 197 globally  
584 distributed buoys along with multi-source remote sensing and reanalysis inputs. The  
585 primary advantage of the BrTHF product is the absence of outliers in the estimation of  
586  $\beta$ . Unlike the approach of our previous study (Wang et al., 2024), which simultaneously  
587 predicted SHF, LHF and  $\beta$  in the constructed RF model, this study employed an NN  
588 model constrained by the Bowen ratio to jointly estimate SHF and LHF. The new  
589 approach avoided the issue of selection of  $\beta$  derived from either the calculated  $\beta$  [ $\beta_{\text{cal}}$   
590 equals predicted SHF ( $\text{SHF}_{\text{pre}}$ ) divided by predicted LHF ( $\text{LHF}_{\text{pre}}$ )] or the predicted  $\beta$   
591 ( $\beta_{\text{pre}}$ ), as reported by Wang et al. (2024). Furthermore, the custom loss function in our  
592 new approach provides a flexible approach to adjust the weights of SHF, LHF, and  $\beta$ ,  
593 allowing the model to balance attention among these variables. As a result, the accuracy  
594 of SHF, LHF, and  $\beta$  from our newly developed BrTHF model outperformed that of the  
595 mainstream air-sea turbulent heat fluxes products and the physics-free NN models on  
596 both global and regional scales. In contrast, the accuracy of SHF and LHF in the model  
597 constructed by Wang et al. (2024) was somewhat marginally lower than that of the  
598 physics-free RF model. The machine learning-based OHF product demonstrated  
599 significantly poorer performance in estimating SHF and LHF, with higher RMSEs and  
600 lower values of  $r$ , as shown in Figure 6, compared to the remote sensing-, reanalysis-,

601 and hybrid-based products developed using the bulk aerodynamic methods. This  
602 finding contrasted with the results of Tang et al. (2024), who reported the superior  
603 performance of the OHF product. The discrepancy could primarily be attributed to the  
604 different spatial representativeness of the observation datasets used by Tang et al.  
605 (2024), which were primarily collected from the buoys between 30°N and 30°S.  
606 Moreover, as shown in Figure 7, the accuracy of the OHF product degraded notably in  
607 high-latitude ocean basins, particularly in the North Atlantic Ocean. This accuracy  
608 degradation may be due to the limitation of the observation datasets used to train the  
609 model of the OHF product, where different sources of datasets were integrated, i.e. the  
610 SeaFlux in-situ dataset (before 2007) and the ICOADS in-situ dataset (after 2007).  
611 Specially, the ICOADS in-situ datasets, commonly used for developing products at  
612 monthly or lower frequency scales (Berry and Kent, 2011; Gulev et al., 2013), suffered  
613 from sparse distribution and insufficient volume for developing the original 3-hour  
614 OHF product. Besides, the model of the OHF product was trained by randomly splitting  
615 all observations into training, validation, and test sets, which likely resulted in data  
616 dependencies across these sets, weakening the model's transferability. These problems  
617 together contributed to the poorer performance of the OHF product, including worse  
618 accuracy, overall negative spatial trends in high-latitude oceans such as the Southern  
619 Ocean, as Tang et al. (2024) reported, and an overall underestimation of the multi-year  
620 mean, especially in the Western Boundary Currents (WBCs) where the air-sea exchange  
621 is intense. In addition, the OHF product did not reproduce similar large-scale spatial  
622 patterns of air–sea turbulent heat fluxes observed in BrTHF, ERA5, and SeaFlux, which  
623 are primarily shaped by atmospheric circulation and sea surface properties (e.g., sea  
624 surface temperature and salinity).

625 Based on Figure 2 and Table S8, we observe that the spatial coverage of  
626 observations varies across different ocean regions: the Northern Hemisphere generally  
627 has higher coverage than the Southern Hemisphere, with the Northern Pacific Ocean  
628 exhibiting the highest coverage, while the Arctic Ocean shows the lowest. Comparing

629 spatial coverage with accuracy metrics reveals a more complex relationship between  
630 model performance and data coverage. Specifically, the values of  $r$  tend to be lower in  
631 regions with lower coverage — a pattern consistent across SHF, LHF, and  $\beta$ . However,  
632 RMSE does not follow this trend. For SHF and  $\beta$ , RMSEs in the Northern Hemisphere  
633 are generally higher than those in the Southern Hemisphere. Similarly, for LHF, RMSEs  
634 are higher in the Northern Hemisphere except in the Indian Ocean, where the pattern  
635 differs.

636 We applied a spatial 10-fold cross-validation, which provides a more generalized  
637 assessment than traditional random cross-validation, to evaluate the BrTHF model.  
638 However, it is important to acknowledge that the spatial distribution of the training  
639 dataset is inherently imbalanced, with a heavy concentration of observations in the  
640 Tropics and the Northern Hemisphere. In contrast, the Southern Hemisphere—  
641 particularly the Southern Ocean—suffers from sparse or even missing observational  
642 coverage. Given that the environmental conditions in these underrepresented or data-  
643 sparse regions may differ significantly from those captured in the training dataset, the  
644 selected input variables for the observations may lead to large uncertainty in the model's  
645 performance in these areas. To further assess the model's ability to extrapolate to such  
646 regions, we conducted an additional targeted cross-validation. Specifically, we  
647 excluded stations from the Southern Ocean [i.e., Southern Ocean Flux Station (SOFS)  
648 and Global Southern Ocean Station (GSOS)] from the training dataset and used them  
649 solely for validation. Results presented in Tables S4 and S5 show that the BrTHF model  
650 achieved the best performance in terms of LHF and  $\beta$  at the SOFS with lower RMSE  
651 of  $15.6 \text{ W/m}^2$  and  $0.73$  and higher values of  $r$  of  $0.96$  and  $0.34$ , respectively, while its  
652 SHF was slightly outperformed by ERA5 and the physics-free NN model. At the GSOS,  
653 BrTHF yielded more accurate estimates for SHF and  $\beta$  with RMSEs of  $6.38 \text{ W/m}^2$  and  
654  $0.74$  and values of  $r$  of  $0.95$  and  $0.16$ , respectively, compared to other products, while  
655 its LHF was marginally less accurate than that of SeaFlux and the physics-free NN  
656 model. Moreover, under both spatially-informed cross-validation and targeted cross-

657 validation, the model demonstrates comparable accuracy at the two sites, as shown in  
658 Figures S4–S7. These findings suggest that BrTHF retains competitive accuracy of SHF,  
659 LHF and  $\beta$  even in regions entirely excluded from training, reflecting promising  
660 generalization. While these results are encouraging, it is important to note that the  
661 validation remains limited to a small number of sites with available observations.  
662 Therefore, the reported  $r$  values and RMSE reflect model performance in these specific  
663 locations and do not necessarily guarantee similar accuracy in broader, unobserved  
664 ocean regions.

665 The generalization capability of the model can also affect the accuracy of  
666 simulated long-term trends. In Figure 13, we present the spatial distributions of long-  
667 term trends for SHF, LHF, and  $\beta$  simulated by the BrTHF product. Considering the  
668 scarcity of training data in high-latitude oceans, the simulated long-term trends in these  
669 regions may be associated with larger uncertainties. However, due to the lack of long-  
670 term observations in high-latitude oceans, we cannot validate the simulated trends using  
671 observational records as has been done in previous studies for mid- and low-latitude  
672 regions (Weller et al., 2022; Tang et al., 2024). To address this, we examined the spatial  
673 distribution of long-term trends from the other seven widely used products. Specifically,  
674 in these high-latitude regions, the trends simulated by the BrTHF are largely consistent  
675 with those of most other products—for example, SHF exhibits a pronounced increase  
676 in the Kara Sea, Gulf Stream, Baffin Bay, Brazil Current, Sea of Okhotsk, and Sea of  
677 Japan, with differences mainly in magnitude.

678 Although the results demonstrated significant improvements in the accuracy and  
679 physical consistency of SHF, LHF, and  $\beta$  estimates from the BrTHF model compared  
680 to those from the physics-free NN models and the seven products, the BrTHF product  
681 also has some limitations. First, due to the lack of an explicitly defined reasonable range  
682 for daily  $\beta$ , the constraint of  $\beta$  used in this study was derived from the daily  $\beta$  global  
683 distribution in the seven widely used global products. While incorporating the  
684 constraint of  $\beta$  into the model effectively suppresses outliers, it also compresses the

685 physically plausible range of  $\beta$ . As a result, the distribution of  $\beta$  shown in Figure 5(i)  
686 differs notably from other products and models, which may limit the product's  
687 applicability for users interested in extreme  $\beta$  values. It is highlighted that although the  
688 BrTHF model slightly underestimates the extreme values of  $\beta$ , it avoids the occurrence  
689 of unrealistic outliers (e.g., 5 to 500 or -5 to -500) seen in other products, making it  
690 overall better aligned with observations. Moving forward, we aim to enhance the  
691 model's ability to preserve physically plausible extremes while maintaining robustness  
692 against outliers in future updates. Secondly, the estimated SHF and LHF values  
693 exhibited a narrower distribution compared to the observations. This issue possibly  
694 stems from the uncertainty of the BrTHF model that was constructed from the uneven  
695 distribution of SHF and LHF in the observation datasets, which contain a low  
696 proportion of extreme samples, especially negative LHF values. Moreover, due to the  
697 insufficient observations, validation and modelling in high-latitude oceans, especially  
698 in the Southern Ocean, was limited. To address these problems, more experiments are  
699 highly recommended to collect observations covering more regions of oceans with  
700 better spatial and temporal representativeness, which could further enhance the product.

701 The BrTHF model demonstrated the feasibility and potential of jointly estimating  
702 multiple interrelated air-sea variables through a machine learning model that  
703 incorporates appropriate physical constraints to account for their interrelations. In the  
704 future, the predicted variables in the BrTHF model could be expanded to include  
705 surface radiation, heat storage, and precipitation over the ocean, by integrating the  
706 physical mechanisms of energy and water exchange. This would allow for the  
707 collaborative optimization of estimates across all components of the air-sea energy and  
708 water budgets, potentially contributing to achieving global closure of the air-sea energy  
709 and water budgets.

710

#### 711 **4. Data and code availability**

712 The daily 0.25° BrTHF product, consisting of SHF and LHF estimates from 1993

713 to 2017, can be freely accessed from the National Tibetan Plateau Data Center (TPDC)  
714 [<https://doi.org/10.11888/Atmos.tpdc.302578>, Tang and Wang (2025)]. The code for  
715 developing the product can be found on the GitHub platform  
716 (<https://github.com/zhezhe1996/BrTHF>).

717

## 718 **5. Summary and Conclusion**

719 In this study, we generated a daily  $0.25^\circ$  air-sea turbulent heat fluxes product for  
720 the period 1993 to 2017 using our developed BrTHF model and multi-source remote  
721 sensing and reanalysis data. A comprehensive validation was performed against  
722 observations from 197 buoys and inter-comparisons were made with seven  
723 representative gridded products. The key findings are as follows:

724 The BrTHF model demonstrated the most significant improvement in estimating  
725 the  $\beta$ , while its performance in estimating SHF and LHF was generally comparable to  
726 or slightly better than that of the physics-free NN models and the seven widely used  
727 air-sea turbulent heat products (including the JOFURO3, IFREMER, SeaFlux, ERA5,  
728 MERRA2, OAFlux and OHF products). Through the spatial ten-fold cross-validation  
729 against the observations from the 197 buoys, the BrTHF model achieved RMSEs of  
730  $6.05 \text{ W/m}^2$  for SHF,  $23.67 \text{ W/m}^2$  for LHF and 0.22 for  $\beta$ , and showed values of  $r$  of 0.93,  
731 0.91, and 0.25 for SHF, LHF, and  $\beta$ , respectively. Additionally, The BrTHF model  
732 performed better in evaluations across six major ocean basins, with lower RMSEs and  
733 higher values of  $r$ , in comparison to the physics-free NN models and the seven products.  
734 Notably, the BrTHF model significantly improved the rationality of  $\beta$  estimates,  
735 successfully eliminating the outliers observed in both the physics-free NN models and  
736 the seven products. Furthermore, the global distributions for SHF, LHF, and  $\beta$  from the  
737 BrTHF product closely matched those of the physically-based ERA5 and SeaFlux  
738 products. The global mean annual estimates of SHF, LHF, and  $\beta$  from the BrTHF  
739 product from 1993 to 2017 were  $12.7 \text{ W/m}^2$ ,  $106.2 \text{ W/m}^2$  and 0.11, respectively, all  
740 within the ranges of the seven products. The BrTHF product exhibited similar intra-

741 annual cycles for SHF, LHF and  $\beta$ , with bimodal patterns featuring lower and higher  
742 peaks in May-June-July-August and December-January, respectively, which was  
743 consistent with the results of the seven state-of-the-art products. Additionally, the  
744 BrTHF product exhibited significant increasing trends for global SHF and LHF, with  
745 rates of 0.04 W/(m<sup>2</sup> year) and 0.33 W/(m<sup>2</sup> year), respectively, which were consistent to  
746 most of the seven products. In contrast, the BrTHF product displayed weak growth in  
747  $\beta$ , with a trend approaching 0, which were opposite to the results of the seven products  
748 except for the MERRA2 product. The increasing (significant increasing) trends  
749 dominated the oceans, with areas of 71.4% (26.2%) for SHF, 87.5% (38.9%) for LHF,  
750 53% (12.2%) for  $\beta$  in the BrTHF product.

751 The BrTHF product shows significant advantages in the accuracy and rationality  
752 of estimates for key parameters (SHF, LHF, and  $\beta$ ) related to air-sea interaction and the  
753 global energy and water budgets compared to the existing products. It holds great  
754 potential for quantifying the global air-sea energy and water budgets, enhancing our  
755 understanding of the air-sea interaction, and projecting climate change under global  
756 warming.

## 757 **Author contribution**

758 YW and RT conceived the study and designed the experimental framework. YW  
759 performed the experiment and prepared the initial manuscript draft. All authors  
760 contributed to manuscript revision, and approved the final version of the manuscript.

## 761 **Competing interests**

762 The contact author has declared that none of the authors has any competing  
763 interests.

## 764 **Acknowledgement**

765 We thank the flux datasets and learning datasets provided by the J-OFURO project,  
766 IFREMER, ECMWF, NASA, WHOI, NOAA, CEMES and RSS. Moreover, we thank

767 the observations provided by the TAO/TRITON, PIRATA, RAMA, NDBC, TAC, UOP,  
768 OOI, AOOS, KOREA, OCS, JKEO and IMO networks or organizations. This work is  
769 supported by the National Natural Science Foundation of China [42271378,42071332],  
770 and the Strategic Priority Research Program of the Chinese Academy of Sciences  
771 (Grant No. XDB0740202).

772

## 773 **References**

- 774 Andreas, E. L., Jordan, R. E., Mahrt, L., and Vickers, D.: Estimating the Bowen ratio  
775 over the open and ice-covered ocean, *Journal of Geophysical Research: Oceans*,  
776 118, 4334-4345, 10.1002/jgrc.20295, 2013.
- 777 Bentamy, A., Piollé, J. F., Grouazel, A., Danielson, R., Gulev, S., Paul, F., Azelmat, H.,  
778 Mathieu, P. P., von Schuckmann, K., Sathyendranath, S., Evers-King, H., Esau, I.,  
779 Johannessen, J. A., Clayson, C. A., Pinker, R. T., Grodsky, S. A., Bourassa, M.,  
780 Smith, S. R., Haines, K., Valdivieso, M., Merchant, C. J., Chapron, B., Anderson,  
781 A., Hollmann, R., and Josey, S. A.: Review and assessment of latent and sensible  
782 heat flux accuracy over the global oceans, *Remote Sensing of Environment*, 201,  
783 196-218, 10.1016/j.rse.2017.08.016, 2017.
- 784 Berry, D. I. and Kent, E. C.: Air-Sea fluxes from ICOADS: the construction of a new  
785 gridded dataset with uncertainty estimates, *International Journal of Climatology*,  
786 31, 987-1001, 10.1002/joc.2059, 2011.
- 787 Bonjean, F. and Lagerloef, G. S.: Diagnostic model and analysis of the surface currents  
788 in the tropical Pacific Ocean, *Journal of Physical Oceanography*, 32, 2938-2954,  
789 2002.
- 790 Bourras, D.: Comparison of five satellite-derived latent heat flux products to moored  
791 buoy data, *Journal of Climate*, 19, 6291-6313, 2006.
- 792 Bourras, D., Eymard, L., and Liu, W. T.: A neural network to estimate the latent heat  
793 flux over oceans from satellite observations, *International Journal of Remote*  
794 *Sensing*, 23, 2405-2423, 10.1080/01431160110070825, 2002.
- 795 Bourras, D., Liu, W. T., Eymard, L., and Tang, W.: Evaluation of latent heat flux fields  
796 from satellites and models during SEMAPHORE, *Journal of Applied Meteorology*,  
797 42, 227-239, 2003.
- 798 Bourras, D., Reverdin, G., Caniaux, G., and Belamari, S.: A Nonlinear Statistical Model  
799 of Turbulent Air-Sea Fluxes, *Monthly Weather Review*, 135, 1077-1089,  
800 10.1175/mwr3335.1, 2007.
- 801 Bourras, D., Cambra, R., Marié, L., Bouin, M. N., Baggio, L., Branger, H., Beghoura,  
802 H., Reverdin, G., Dewitte, B., Paulmier, A., Maes, C., Arduin, F., Pairaud, I.,  
803 Fraunié, P., Luneau, C., and Hauser, D.: Air - Sea Turbulent Fluxes From a  
804 Wave - Following Platform During Six Experiments at Sea, *Journal of*  
805 *Geophysical Research: Oceans*, 124, 4290-4321, 10.1029/2018jc014803, 2019.

806 Bourras, D., Weill, A., Caniaux, G., Eymard, L., Bourlès, B., Letourneur, S., Legain,  
807 D., Key, E., Baudin, F., Piguet, B., Traullé, O., Bouhours, G., Sinardet, B., Barrié,  
808 J., Vinson, J. P., Boutet, F., Berthod, C., and Cléménçon, A.: Turbulent air - sea  
809 fluxes in the Gulf of Guinea during the AMMA experiment, *Journal of*  
810 *Geophysical Research: Oceans*, 114, 10.1029/2008jc004951, 2009.

811 Brodeau, L., Barnier, B., Gulev, S. K., and Woods, C.: Climatologically Significant  
812 Effects of Some Approximations in the Bulk Parameterizations of Turbulent Air–  
813 Sea Fluxes, *Journal of Physical Oceanography*, 47, 5-28, 10.1175/jpo-d-16-0169.1,  
814 2017.

815 Brunke, M. A.: Uncertainties in sea surface turbulent flux algorithms and data sets,  
816 *Journal of Geophysical Research*, 107, 10.1029/2001jc000992, 2002.

817 Cai, L., Wang, B., Wang, W., and Feng, X.: The Impact of Air–Sea Flux  
818 Parameterization Methods on Simulating Storm Surges and Ocean Surface  
819 Currents, *Journal of Marine Science and Engineering*, 13, 10.3390/jmse13030541,  
820 2025.

821 Chen, X., Yao, Y., Zhao, S., Li, Y., Jia, K., Zhang, X., Shang, K., Xu, J., and Bei, X.:  
822 Estimation of High-Resolution Global Monthly Ocean Latent Heat Flux from  
823 MODIS SST Product and AMSR-E Data, *Advances in Meteorology*, 2020, 1-19,  
824 10.1155/2020/8857618, 2020a.

825 Chen, X., Yao, Y., Li, Y., Zhang, Y., Jia, K., Zhang, X., Shang, K., Yang, J., Bei, X., and  
826 Guo, X.: ANN-Based Estimation of Low-Latitude Monthly Ocean Latent Heat  
827 Flux by Ensemble Satellite and Reanalysis Products, *Sensors (Basel)*, 20,  
828 10.3390/s20174773, 2020b.

829 Clayson, C. and Brown, J.: NOAA Climate Data Record Ocean Surface Bundle (OSB)  
830 Climate Data Record (CDR) of Ocean Heat Fluxes, Version 2, *Clim. Algorithm*  
831 *Theor. Basis Doc. C-ATBD Asheville NC NOAA Natl. Cent. Environ. Inf. Doi*,  
832 10, V59K4885, 2016.

833 Crespo, J., Posselt, D., and Asharaf, S.: CYGNSS Surface Heat Flux Product  
834 Development, *Remote Sensing*, 11, 10.3390/rs11192294, 2019.

835 Cummins, D. P., Guemas, V., Cox, C. J., Gallagher, M. R., and Shupe, M. D.: Surface  
836 Turbulent Fluxes From the MOSAiC Campaign Predicted by Machine Learning,  
837 *Geophysical Research Letters*, 50, 10.1029/2023gl105698, 2023.

838 Cummins, D. P., Guemas, V., Blein, S., Brooks, I. M., Renfrew, I. A., Elvidge, A. D.,  
839 and Prytherch, J.: Reducing Parametrization Errors for Polar Surface Turbulent  
840 Fluxes Using Machine Learning, *Boundary-Layer Meteorology*, 190,  
841 10.1007/s10546-023-00852-8, 2024.

842 Edson, J. B. a. J., Venkata and Weller, Robert A and Bigorre, Sebastien P and  
843 Plueddemann, Albert J and Fairall, Christopher W and Miller, Scott D and Mahrt,  
844 Larry and Vickers, Dean and Hersbach, Hans: On the Exchange of Momentum  
845 over the Open Ocean, *Journal of Physical Oceanography*, 43, 1589-1610,  
846 10.1175/jpo-d-12-0173.1, 2013.

847 Fasullo, J. T., Trenberth, K. E., and Balmaseda, M. A.: Earth’s Energy Imbalance,

848 Journal of Climate, 27, 3129-3144, 10.1175/jcli-d-13-00294.1, 2014.

849 Fu, S., Huang, W., Luo, J., Yang, Z., Fu, H., Luo, Y., and Wang, B.: Deep Learning -  
850 Based Sea Surface Roughness Parameterization Scheme Improves Sea Surface  
851 Wind Forecast, *Geophysical Research Letters*, 50, 10.1029/2023gl106580, 2023.

852 Gentemann, C. L., Clayson, C. A., Brown, S., Lee, T., Parfitt, R., Farrar, J. T., Bourassa,  
853 M., Minnett, P. J., Seo, H., Gille, S. T., and Zlotnicki, V.: FluxSat: Measuring the  
854 Ocean–Atmosphere Turbulent Exchange of Heat and Moisture from Space,  
855 *Remote Sensing*, 12, 10.3390/rs12111796, 2020.

856 Grist, J. P., Josey, S. A., Zika, J. D., Evans, D. G., and Skliris, N.: Assessing recent air-  
857 sea freshwater flux changes using a surface temperature-salinity space framework,  
858 *Journal of Geophysical Research: Oceans*, 121, 8787-8806,  
859 10.1002/2016jc012091, 2016.

860 Gulev, S. K., Latif, M., Keenlyside, N., Park, W., and Koltermann, K. P.: North Atlantic  
861 Ocean control on surface heat flux on multidecadal timescales, *Nature*, 499, 464-  
862 467, 10.1038/nature12268, 2013.

863 Hersbach, H., Bell, B., Berrisford, P., Hirahara, S., Horányi, A., Muñoz - Sabater, J.,  
864 Nicolas, J., Peubey, C., Radu, R., Schepers, D., Simmons, A., Soci, C., Abdalla,  
865 S., Abellan, X., Balsamo, G., Bechtold, P., Biavati, G., Bidlot, J., Bonavita, M.,  
866 Chiara, G., Dahlgren, P., Dee, D., Diamantakis, M., Dragani, R., Flemming, J.,  
867 Forbes, R., Fuentes, M., Geer, A., Haimberger, L., Healy, S., Hogan, R. J., Hólm,  
868 E., Janisková, M., Keeley, S., Laloyaux, P., Lopez, P., Lupu, C., Radnoti, G.,  
869 Rosnay, P., Rozum, I., Vamborg, F., Villaume, S., and Thépaut, J. N.: The ERA5  
870 global reanalysis, *Quarterly Journal of the Royal Meteorological Society*, 146,  
871 1999-2049, 10.1002/qj.3803, 2020.

872 Huang, B., Liu, C., Banzon, V., Freeman, E., Graham, G., Hankins, B., Smith, T., and  
873 Zhang, H.-M.: Improvements of the Daily Optimum Interpolation Sea Surface  
874 Temperature (DOISST) Version 2.1, *Journal of Climate*, 34, 2923-2939,  
875 10.1175/jcli-d-20-0166.1, 2021.

876 Jiang, Y., Li, Y., Lu, Y., Wu, T., and Gao, Z.: Evaluating modifications to air–sea  
877 momentum flux parameterizations under light wind conditions in CAM6, *Climate  
878 Dynamics*, 62, 9687-9701, 10.1007/s00382-024-07415-8, 2024a.

879 Jiang, Y., Li, Y., Lu, Y., Wu, T., Zhang, J., and Gao, Z.: Evaluating nine different air-sea  
880 flux algorithms coupled with CAM6, *Atmospheric Research*,  
881 10.1016/j.atmosres.2024.107486, 2024b.

882 Jo, Y.-H.: Calculation of the Bowen ratio in the tropical Pacific using sea surface  
883 temperature data, *Journal of Geophysical Research*, 107, 10.1029/2001jc001150,  
884 2002.

885 Karniadakis, G. E., Kevrekidis, I. G., Lu, L., Perdikaris, P., Wang, S., and Yang, L.:  
886 Physics-informed machine learning, *Nature Reviews Physics*, 3, 422-440, 2021.

887 Kashinath, K., Mustafa, M., Albert, A., Wu, J., Jiang, C., Esmailzadeh, S.,  
888 Azizzadenesheli, K., Wang, R., Chattopadhyay, A., and Singh, A.: Physics-  
889 informed machine learning: case studies for weather and climate modelling,

890 Philosophical Transactions of the Royal Society A, 379, 20200093, 2021.

891 Kudryavtsev, V., Chapron, B., and Makin, V.: Impact of wind waves on the air - sea  
892 fluxes: A coupled model, *Journal of Geophysical Research: Oceans*, 119, 1217-  
893 1236, 10.1002/2013jc009412, 2014.

894 Liman, J., Schröder, M., Fennig, K., Andersson, A., and Hollmann, R.: Uncertainty  
895 characterization of HOAPS 3.3 latent heat-flux-related parameters, *Atmospheric  
896 Measurement Techniques*, 11, 1793-1815, 10.5194/amt-11-1793-2018, 2018.

897 Liu, Z. and Yang, H.: Estimation of Water Surface Energy Partitioning With a  
898 Conceptual Atmospheric Boundary Layer Model, *Geophysical Research Letters*,  
899 48, 10.1029/2021gl092643, 2021.

900 Loeb, N. G., Johnson, G. C., Thorsen, T. J., Lyman, J. M., Rose, F. G., and Kato, S.:  
901 Satellite and Ocean Data Reveal Marked Increase in Earth's Heating Rate,  
902 *Geophysical Research Letters*, 48, 10.1029/2021GL093047, 2021.

903 Monin, A. S. and Obukhov, A. M.: Basic laws of turbulent mixing in the surface layer  
904 of the atmosphere, *Contrib. Geophys. Inst. Acad. Sci. USSR*, 151, e187, 1954.

905 Myslenkov, S., Shestakova, A., and Chechin, D.: The impact of sea waves on turbulent  
906 heat fluxes in the Barents Sea according to numerical modeling, *Atmospheric  
907 Chemistry and Physics*, 21, 5575-5595, 10.5194/acp-21-5575-2021, 2021.

908 Nelson, J. A., Walther, S., Gans, F., Kraft, B., Weber, U., Novick, K., Buchmann, N.,  
909 Migliavacca, M., Wohlfahrt, G., Šigut, L., Ibrom, A., Papale, D., Göckede, M.,  
910 Duveiller, G., Knohl, A., Hörtnagl, L., Scott, R. L., Zhang, W., Hamdi, Z. M.,  
911 Reichstein, M., Aranda-Barranco, S., Ardö, J., Op de Beeck, M., Billesbach, D.,  
912 Bowling, D., Bracho, R., Brümmer, C., Camps-Valls, G., Chen, S., Cleverly, J. R.,  
913 Desai, A., Dong, G., El-Madany, T. S., Euskirchen, E. S., Feigenwinter, I.,  
914 Galvagno, M., Gerosa, G. A., Gielen, B., Goded, I., Goslee, S., Gough, C. M.,  
915 Heinesch, B., Ichii, K., Jackowicz-Korczynski, M. A., Klosterhalfen, A., Knox, S.,  
916 Kobayashi, H., Kohonen, K.-M., Korkiakoski, M., Mammarella, I., Gharun, M.,  
917 Marzuoli, R., Matamala, R., Metzger, S., Montagnani, L., Nicolini, G., O'Halloran,  
918 T., Ourcival, J.-M., Peichl, M., Pendall, E., Ruiz Reverter, B., Roland, M.,  
919 Sabbatini, S., Sachs, T., Schmidt, M., Schwalm, C. R., Shekhar, A., Silberstein, R.,  
920 Silveira, M. L., Spano, D., Tagesson, T., Tramontana, G., Trotta, C., Turco, F.,  
921 Vesala, T., Vincke, C., Vitale, D., Vivoni, E. R., Wang, Y., Woodgate, W., Yopez,  
922 E. A., Zhang, J., Zona, D., and Jung, M.: X-BASE: the first terrestrial carbon and  
923 water flux products from an extended data-driven scaling framework,  
924 *FLUXCOM-X, Biogeosciences*, 21, 5079-5115, 10.5194/bg-21-5079-2024, 2024.

925 O, S. and Orth, R.: Global soil moisture data derived through machine learning trained  
926 with in-situ measurements, *Sci Data*, 8, 170, 10.1038/s41597-021-00964-1, 2021.

927 Peng, Z., Tang, R., Jiang, Y., Liu, M., and Li, Z.-L.: Global estimates of 500 m daily  
928 aerodynamic roughness length from MODIS data, *ISPRS Journal of  
929 Photogrammetry and Remote Sensing*, 183, 336-351,  
930 10.1016/j.isprsjprs.2021.11.015, 2022.

931 Petersen, G. N.: Meteorological buoy measurements in the Iceland Sea, 2007–2009,

932 Earth System Science Data, 9, 779-789, 10.5194/essd-9-779-2017, 2017.

933 Robertson, F. R., Roberts, J. B., Bosilovich, M. G., Bentamy, A., Clayson, C. A., Fennig,  
934 K., Schröder, M., Tomita, H., Compo, G. P., Gutenstein, M., Hersbach, H.,  
935 Kobayashi, C., Ricciardulli, L., Sardeshmukh, P., and Slivinski, L. C.:  
936 Uncertainties in Ocean Latent Heat Flux Variations over Recent Decades in  
937 Satellite-Based Estimates and Reduced Observation Reanalyses, *Journal of*  
938 *Climate*, 33, 8415-8437, 10.1175/jcli-d-19-0954.1, 2020.

939 Shang, K., Yao, Y., Di, Z., Jia, K., Zhang, X., Fisher, J. B., Chen, J., Guo, X., Yang, J.,  
940 Yu, R., Xie, Z., Liu, L., Ning, J., and Zhang, L.: Coupling physical constraints with  
941 machine learning for satellite-derived evapotranspiration of the Tibetan Plateau,  
942 *Remote Sensing of Environment*, 289, 10.1016/j.rse.2023.113519, 2023.

943 Shie, C.-L., Chiu, L. S., Adler, R., Nelkin, E., Lin, I. I., Xie, P., Wang, F.-C.,  
944 Chokngamwong, R., Olson, W., and Chu, D. A.: A note on reviving the Goddard  
945 Satellite-based Surface Turbulent Fluxes (GSSTF) dataset, *Advances in*  
946 *Atmospheric Sciences*, 26, 1071-1080, 10.1007/s00376-009-8138-z, 2009.

947 Song, X.: The Importance of Relative Wind Speed in Estimating Air–Sea Turbulent  
948 Heat Fluxes in Bulk Formulas: Examples in the Bohai Sea, *Journal of Atmospheric*  
949 *and Oceanic Technology*, 37, 589-603, 10.1175/jtech-d-19-0091.1, 2020.

950 Song, X.: The Importance of Including Sea Surface Current when Estimating Air–Sea  
951 Turbulent Heat Fluxes and Wind Stress in the Gulf Stream Region, *Journal of*  
952 *Atmospheric and Oceanic Technology*, 38, 119-138, 10.1175/jtech-d-20-0094.1,  
953 2021.

954 Song, X., Xie, X., Yan, Y., and Xie, S.-P.: Observed sub-daily variations in air–sea  
955 turbulent heat fluxes under different marine atmospheric boundary layer stability  
956 conditions in the Gulf Stream, *Monthly Weather Review*, 10.1175/mwr-d-24-  
957 0003.1, 2024.

958 TANG, R. and WANG, Y.: Global dataset of air-sea turbulent heat fluxes (sensible heat  
959 flux and latent heat flux) (1993–2017), National Tibetan Plateau Data Center  
960 [dataset], <https://dx.doi.org/10.11888/Atmos.tpcd.302578>, 2025.

961 Tang, R., Wang, Y., Jiang, Y., Liu, M., Peng, Z., Hu, Y., Huang, L., and Li, Z.-L.: A  
962 review of global products of air-sea turbulent heat flux: accuracy, mean, variability,  
963 and trend, *Earth-Science Reviews*, 249, 10.1016/j.earscirev.2023.104662, 2024.

964 Tomita, H., Hihara, T., Kako, S. i., Kubota, M., and Kutsuwada, K.: An introduction to  
965 J-OFURO3, a third-generation Japanese ocean flux data set using remote-sensing  
966 observations, *Journal of Oceanography*, 75, 171-194, 10.1007/s10872-018-0493-  
967 x, 2018.

968 van der Westhuizen, S., Heuvelink, G. B., and Hofmeyr, D. P.: Multivariate random  
969 forest for digital soil mapping, *Geoderma*, 431, 116365, 2023.

970 Wang, J., Tang, R., Jiang, Y., Liu, M., and Li, Z.-L.: A practical method for angular  
971 normalization of global MODIS land surface temperature over vegetated surfaces,  
972 *ISPRS Journal of Photogrammetry and Remote Sensing*, 199, 289-304,  
973 10.1016/j.isprsjprs.2023.04.015, 2023.

974 Wang, Y., Tang, R., Huang, L., Liu, M., Jiang, Y., and Li, Z.-L.: A Bowen ratio-informed  
975 method for coordinating the estimates of air–sea turbulent heat fluxes,  
976 *Environmental Research Letters*, 19, 10.1088/1748-9326/ad9341, 2024.

977 Weller, R. A., Lukas, R., Potemra, J., Plueddemann, A. J., Fairall, C., and Bigorre, S.:  
978 Ocean Reference Stations: Long-Term, Open-Ocean Observations of Surface  
979 Meteorology and Air–Sea Fluxes Are Essential Benchmarks, *Bulletin of the*  
980 *American Meteorological Society*, 103, E1968-E1990, 10.1175/bams-d-21-0084.1,  
981 2022.

982 Wild, M., Folini, D., Hakuba, M. Z., Schär, C., Seneviratne, S. I., Kato, S., Rutan, D.,  
983 Ammann, C., Wood, E. F., and König-Langlo, G.: The energy balance over land  
984 and oceans: an assessment based on direct observations and CMIP5 climate  
985 models, *Climate Dynamics*, 44, 3393-3429, 10.1007/s00382-014-2430-z, 2014.

986 Yan, Y., Song, X., Wang, G., and Li, X.: Tropical Cool-Skin and Warm-Layer Effects  
987 and Their Impact on Surface Heat Fluxes, *Journal of Physical Oceanography*, 54,  
988 45-62, 10.1175/jpo-d-23-0103.1, 2024.

989 Yang, Y., Sun, H., Wang, J., Zhang, W., Zhao, G., Wang, W., Cheng, L., Chen, L., Qin,  
990 H., and Cai, Z.: Global ocean surface heat fluxes revisited: A new dataset from  
991 maximum entropy production framework with heat storage and Bowen ratio  
992 optimizations, *Earth System Science Data Discussions*, 2024, 1-44, 2024.

993 Yu, L.: Global Air–Sea Fluxes of Heat, Fresh Water, and Momentum: Energy Budget  
994 Closure and Unanswered Questions, *Annual Review of Marine Science*, 11, 227-  
995 248, 10.1146/annurev-marine-010816-060704, 2019.

996 Yu, L. and Weller, R. A.: Objectively Analyzed Air–Sea Heat Fluxes for the Global Ice-  
997 Free Oceans (1981–2005), *Bulletin of the American Meteorological Society*, 88,  
998 527-540, 10.1175/bams-88-4-527, 2007.

999 Zhang, R., Guo, Weihao, Wang, Xin, and Wang, Chunzai: Ambiguous Variations in  
1000 Tropical Latent Heat Flux since the Years around 1998, *Journal of Climate*, 36,  
1001 3403–3415, 2023.

1002 Zhao, W. L., Gentine, P., Reichstein, M., Zhang, Y., Zhou, S., Wen, Y., Lin, C., Li, X.,  
1003 and Qiu, G. Y.: Physics - Constrained Machine Learning of Evapotranspiration,  
1004 *Geophysical Research Letters*, 46, 14496-14507, 10.1029/2019gl085291, 2019.

1005 Zhou, S., Shi, R., Yu, H., Zhang, X., Dai, J., Huang, X., and Xu, F.: A Physical -  
1006 Informed Neural Network for Improving Air - Sea Turbulent Heat Flux  
1007 Parameterization, *Journal of Geophysical Research: Atmospheres*, 129,  
1008 10.1029/2023jd040603, 2024.

1009 Zhou, X., Ray, P., Barrett, B. S., and Hsu, P.-C.: Understanding the bias in surface latent  
1010 and sensible heat fluxes in contemporary AGCMs over tropical oceans, *Climate*  
1011 *Dynamics*, 55, 2957-2978, 10.1007/s00382-020-05431-y, 2020.

1012